



## Modeling global indices for estimating non-photosynthetic vegetation cover

Philip E. Dennison<sup>a,\*</sup>, Brian T. Lamb<sup>b</sup>, Michael J. Campbell<sup>a</sup>, Raymond F. Kokaly<sup>c</sup>,  
W. Dean Hively<sup>j</sup>, Eric Vermote<sup>d</sup>, Phil Dabney<sup>d</sup>, Guy Serbin<sup>e</sup>, Miguel Quemada<sup>f</sup>,  
Craig S.T. Daughtry<sup>g</sup>, Jeffery Masek<sup>h</sup>, Zhuoting Wu<sup>i</sup>

<sup>a</sup> Department of Geography, University of Utah, Salt Lake City, UT 84112, USA

<sup>b</sup> U.S. Geological Survey, Lower Mississippi-Gulf Water Science Center, 2045 Route 112 Building 4, Coram, NY 11727, USA

<sup>c</sup> U.S. Geological Survey, Geology, Geophysics, and Geochemistry Science Center, MS 973 Box 25046, Denver Federal Center, Denver, CO 80225, USA

<sup>d</sup> Biospheric Sciences Laboratory, NASA Goddard Space Flight Center, Greenbelt, MD 20771, USA

<sup>e</sup> EOanalytics Ltd, Talent Garden Dublin, DCU Alpha, Glasnevin, Dublin 11, D11YNR2, Ireland

<sup>f</sup> Universidad Politécnica de Madrid-CEIGRAM, 13 Paseo Senda del Rey, 28040, Madrid, Spain

<sup>g</sup> USDA Agricultural Research Service, Hydrology and Remote Sensing Laboratory (retired), Beltsville, MD 20705, USA

<sup>h</sup> Biospheric Sciences Laboratory, NASA Goddard Space Flight Center (retired), Greenbelt, MD 20771, USA

<sup>i</sup> U.S. Geological Survey, National Land Imaging Program, 2255 N Gemini Dr, Flagstaff, AZ 86001, USA

<sup>j</sup> U.S. Geological Survey, Lower Mississippi-Gulf Water Science Center, Bldg 007, Rm 104, BARC-West, Beltsville, MD 20705, USA

### ARTICLE INFO

Edited by Jing M. Chen

#### Keywords:

NPV  
Litter  
Crop residue  
Lignocellulose absorption  
Spectral mixing  
Index optimization

### ABSTRACT

Non-photosynthetic vegetation (NPV) includes plant litter, senesced leaves, and crop residues. NPV plays an essential role in terrestrial ecosystem processes, and is an important indicator of drought severity, ecosystem disturbance, agricultural resilience, and wildfire danger. Current moderate spatial resolution multispectral satellite systems (e.g., Landsat and Sentinel-2) have only a single band in the 2000–2500 nm shortwave infrared “SWIR2” range where non-pigment biochemical constituents of NPV, including cellulose and lignin, have important spectral absorption features. Thus, these current systems have suboptimal capabilities for characterizing NPV cover. This research used simulated spectral mixtures accounting for variability among NPV and soils to evaluate globally-appropriate hyperspectral and multispectral indices for estimation of fractional NPV cover. The Continuum Interpolated NPV Depth Index (CINDI), a weighted ratio index measuring lignocellulose absorption near 2100 nm, was found to produce the lowest error in estimating NPV cover. CINDI was less sensitive to variability in soil spectra and green vegetation cover than competing indices. While CINDI was sensitive to the relative water content of soil and NPV, this sensitivity allowed for correcting error in estimated NPV cover as water content increased. CINDI bands were less capable than Dual Absorption NPV Index (DANI) bands for maintaining continuity with the heritage Landsat SWIR2 band, but combining multiple CINDI bands demonstrated adequate continuity. Three SWIR2 bands with band centers at 2038, 2108, and 2211 nm can provide superior capabilities for future moderate resolution multispectral/superspectral systems targeting NPV monitoring, including the next generation Landsat mission (Landsat Next). These bands and the associated CINDI index provide potential for global NPV monitoring using a constellation of future superspectral sensors and imaging spectrometers, with applications including improving soil management, preventing land degradation, evaluating impacts of drought, mapping ecosystem disturbance, and assessing wildfire danger.

### 1. Introduction

Non-photosynthetic vegetation (NPV) includes plant litter, senesced leaves, and crop residues, as well as plant organs containing a low concentration of chlorophyll, such as branches, stems, bark, and cones (Daughtry, 2001; Nagler et al., 2000; Roberts et al., 1993). NPV plays an

essential role in terrestrial ecosystem processes by directly impacting carbon and nutrient cycling (Hobbie, 2015). NPV is a powerful indicator of drought severity, and increases in response to ecosystem disturbances like insect outbreaks and extreme weather events (Chambers et al., 2007; Coates et al., 2015; Tane et al., 2018). Seasonal changes in NPV are an important indicator of plant senescence and wildfire danger

\* Corresponding author.

E-mail address: [dennison@geog.utah.edu](mailto:dennison@geog.utah.edu) (P.E. Dennison).

<https://doi.org/10.1016/j.rse.2023.113715>

Received 22 March 2023; Received in revised form 5 July 2023; Accepted 8 July 2023

0034-4257/© 2023 Elsevier Inc. All rights reserved.

(Elmore et al., 2005; Okin, 2010; Roberts et al., 2006). NPV also serves as an important indicator of rangeland vegetation condition, cropland tillage intensity, and erosion potential in agricultural ecosystems (Blanco-Canqui and Wortmann, 2020; Lal, 1995; Marsett et al., 2006). Despite the ecological and societal importance of NPV, satellite remote sensing metrics used for quantifying terrestrial ecosystem processes, mapping land cover change, and monitoring agricultural lands have been more commonly based on the spectral features of photosynthesizing “green” vegetation (GV) than on NPV (Okin, 2010).

NPV is principally made up of cellulose and lignin. These two structural components are the most abundant molecules produced by photosynthetic activity of terrestrial vegetation and have prominent absorption features in the shortwave infrared (SWIR) near 2100 and 2300 nm (Elvidge, 1990). What is commonly referred to as “lignocellulose absorption” is actually a composite of overlapping absorption features caused by overtones and combinations of the fundamental absorptions by molecular bonds in cellulose, lignin, carbohydrates, lipids, and other non-pigment biochemicals making up plant materials. Absorption features produced by these biochemicals are most prevalent in the “SWIR2” spectral region (2000–2500 nm). While plant biochemical absorptions combine to produce the two broad lignocellulose absorption features in the SWIR2 spectral region, absorption feature positions and shapes vary with differing concentrations and chemical compositions of absorbing biochemicals (Kokaly and Clark, 1999). Biochemical concentration and composition can vary across scales, but systemic differences in absorption features have been documented, such as between low-lignin content grass species and high-lignin content pine species (Kokaly et al., 2009). Water in plant tissues can alter or obscure the 2100 nm lignocellulose absorption feature (Kokaly et al., 2013). Vibrational absorption features are not restricted to organic molecules; minerals in background soils, sediments, and rocks also have strong absorption features in the SWIR2 spectral region (Clark, 1999), complicating the use of lignocellulose absorption for estimation of NPV cover.

Despite the complexity of biochemical and mineral absorptions within the SWIR2 spectral region, current moderate spatial resolution multispectral satellite systems (e.g., Landsat, Sentinel-2) have a single, broad band centered near 2200 nm. This single band is not well positioned with respect to lignocellulose absorption maxima near 2100 and 2300 nm, but is still somewhat sensitive to spectral absorption produced by NPV cover. Early Landsat NPV studies focused on identifying differences in crop residue cover, a proxy measure for tillage intensity. Van Deventer et al. (1997) used Landsat 5 Thematic Mapper bands 5 (~1550–1750 nm) and 7 (~2080–2350 nm) to calculate the Normalized Difference Tillage Index (NDTI) and achieved high classification accuracies for identifying fields with low and high crop residue cover. NDTI calculated from Landsat and Sentinel-2 imagery has been used to characterize crop residue cover in many studies and is currently a de facto standard approach (Azzari et al., 2019; Beeson et al., 2020; Hively et al., 2019; Jin et al., 2015; Najafi et al., 2019; Quemada et al., 2018; Zheng et al., 2013). NPV characterization studies applying spectral mixture analysis (SMA) techniques to Landsat 5–9 imagery have produced fairly accurate results across numerous study domains including agricultural fields, pasture, shrublands, forest, and even the continent of Australia (Davidson et al., 2008; Guerschman et al., 2015; Laamrani et al., 2020; Mayes et al., 2015; Numata et al., 2007; Quintano et al., 2013; Scarth et al., 2022). While NPV studies utilizing imagery with a single SWIR2 band have achieved moderate-to-high accuracy results, these studies were often conducted at local to regional scales, and comparisons of their findings reveals inconsistencies at continental and global scales. For example, comparison of studies by Jin et al. (2015), Hively et al. (2018), and Najafi et al. (2019) shows NDTI values varying substantially for the same crop residue cover values for study sites in China, the U.S., and Iran, respectively. This indicates a lack of stability in NDTI relationships with NPV cover, making NDTI unsuitable for global mapping of agricultural NPV cover.

Studies comparing NPV characterization performance for approaches using a single SWIR2 band versus multiple SWIR2 bands have consistently demonstrated higher performance for the latter case (Bannari et al., 2006; Daughtry, 2001; Daughtry et al., 2006; Hively et al., 2018, 2021; Lamb et al., 2022; Quemada et al., 2018; Quemada and Daughtry, 2016; Serbin et al., 2009b; Yue et al., 2019). Serbin et al. (2009b) developed the Shortwave Infrared Normalized Difference Residue Index (SINDRI) with bands centered at 2210 nm and 2260 nm and evaluated its performance across six U.S. sites. They found that SINDRI mapped crop residue cover with an  $R^2 = 0.743$  while NDTI achieved an  $R^2 = 0.299$ . Perhaps the most commonly used NPV index with multiple bands in the SWIR2 spectral region is the Cellulose Absorption Index (CAI), a three-band difference index with band centers at 2000, 2100, and 2200 nm (Nagler et al., 2000). CAI has been demonstrated to accurately characterize NPV across natural ecosystems and agricultural systems alike (Bai et al., 2021; Nagler et al., 2003; Pancorbo et al., 2023; Ren et al., 2012). Daughtry et al. (2006) found that CAI predicted crop residue cover values with an  $R^2$  of 0.774 while NDTI produced an  $R^2$  of 0.108. These studies have established that NPV characterization approaches incorporating a single broad SWIR2 band (e.g., NDTI) are far more prone to errors from variability in GV cover, surface moisture, and soil properties.

Though CAI, SINDRI, and related SWIR2 indices offer good site-scale performance for NPV cover estimation, the availability of imagery capable of computing these indices is limited to a small number of “superspectral” systems (e.g., WorldView-3) or airborne and satellite imaging spectrometers, both with limited spatial footprints. Perhaps related to the limited spatial and temporal coverage provided by these systems, uncertainties remain for optimal placement of spectral bands for NPV cover estimation. For example, the original derivation of the CAI in Nagler et al. (2000) was based on lab spectra and subsequent field studies have found that shifting CAI’s first band to 2019 nm (Daughtry, 2001), 2031 nm (Daughtry et al., 2005), 2036 nm (Lamb et al., 2022), or 2040 nm (Hively et al., 2021) may offer similar performance for NPV cover estimation while mitigating atmospheric interference. Most importantly, past efforts have been based on a limited number of sites and have not included global spectral variability in NPV or soils.

With next generation Landsat and Sentinel-2 multispectral satellite systems currently being developed, there is an opportunity to add multiple SWIR2 bands for more accurately estimating and monitoring NPV cover. For example, the next generation Landsat mission (referred to as “Landsat Next”) is being designed with 26 spectral bands, more than doubling the number of bands measured by Landsats 8 and 9 (US Geological Survey, 2023). The objectives of this analysis are to investigate spectral indices and SWIR2 band combinations for estimation of fractional NPV cover; incorporate variability in NPV and soil reflectance using field and lab spectral libraries to produce indices and bands that should have lower error for global application; characterize the sensitivity of the best indices to factors like soil spectral absorptions, GV cover, and soil/NPV relative water content; and examine potential impacts of best indices on continuity with heritage multispectral systems.

## 2. Methods

Our methodology is divided into three primary sections, illustrated in Fig. 1. Section 2.1 (Synthetic mixtures) details the creation of random linear mixtures using endmembers derived from diverse field and lab spectral libraries. Section 2.2 (Index comparison) describes our methodology for calculating and comparing a wide range of hyperspectral and multispectral indices, arriving at two candidate indices that result in the lowest root mean square error (RMSE) for estimating fractional NPV cover. Section 2.3 (Sensitivity analyses) explains a variety of tests we performed on the most promising multispectral indices.

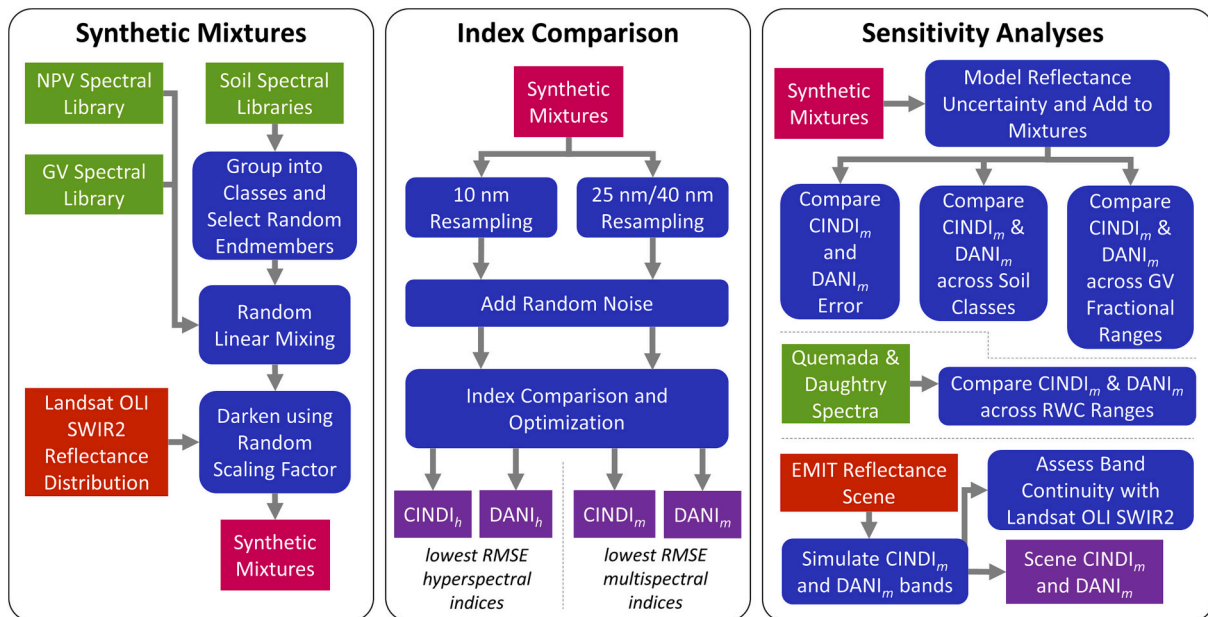


Fig. 1. A flowchart depicting the methodology used in this work. Field and lab spectral data are green, Landsat and EMIT image data are red, the synthetic mixture dataset is magenta, and indices are violet. CINDI and DANI indices are defined in Results sections 3.1 and 3.2.

2.1. Synthetic mixtures

2.1.1. Spectral libraries

Synthetic mixtures of NPV, soil, and GV were derived based on spectral libraries assembled from multiple sources representing each endmember type. To ensure that each endmember represented “pure” cover of NPV, soil, or GV, most spectra were obtained from laboratory or field spectrometer measurements. Some spectra had missing data or very noisy reflectance values beyond 2400 nm, restricting the range of our analysis to 2000–2400 nm. Table 1 describes the provenance of twelve NPV spectra and six GV endmembers. NPV endmembers were selected

from six sources to include both natural NPV cover and agricultural crop residues. Crop residue spectra were also selected to span a range of crop types and relative water content (RWC). Actual bandpass of spectrometers used to measure NPV and GV endmembers is approximately 10–12 nm in the SWIR2 spectral region, depending on model (Dennison et al., 2019). All NPV endmembers were originally oversampled at 1 nm, except for u9litt1a-av which was originally oversampled at 2 nm and then interpolated to 1 nm. NPV and subsequent endmembers provided as relative reflectance were corrected to absolute reflectance by multiplying each spectrum by the reflectance spectrum of the reference panel, a Spectralon® 99% reflective surface.

Table 1  
NPV and GV spectra selected as representing pure endmembers.

Name	Type	Target	Description	Source	Reference
COP_20160526_5-40-W	NPV	grass	dry grass, 99.5% NPV as assessed by photo classification	Field	Dennison et al. (2019)
LL-1-87y	NPV	litter	deciduous leaf litter, leaf stack	Lab	Meerdink et al. (2019)
LL-2-89z	NPV	litter	deciduous leaf litter, leaf stack	Lab	Meerdink et al. (2019)
spec1418-1421	NPV	residue	<i>Glycine max</i> (soy) residue, 0.272 RWC	Lab	Serbin et al. (2009a)
spec172-175	NPV	residue	<i>Triticum aestivum</i> (wheat) residue, old, 0.436 RWC	Lab	Serbin et al. (2009a)
spec300-303	NPV	residue	<i>Glycine max</i> (soy) residue, 0.477 RWC	Lab	Serbin et al. (2009a)
spec308-311	NPV	residue	<i>Triticum aestivum</i> (wheat) residue, new, 0.104 RWC	Lab	Serbin et al. (2009a)
spec356-359	NPV	residue	<i>Zea mays</i> (corn) residue, 0.493 RWC	Lab	Serbin et al. (2009a)
T3.01.E	NPV	residue	<i>Zea mays</i> (corn) residue, 98% residue cover, 0.0131 litter RWC, field of view assessed by photograph point sampling	Field	Quemada and Daughtry (2016)
u9litt1a-av	NPV	litter	<i>Pseudotsuga menziesii</i> (Douglas fir) litter	Field	Roberts et al. (2004)
VH322	NPV	litter	<i>Pinus ponderosa</i> (ponderosa pine) needles	Lab	Meerdink et al. (2019)
VH358	NPV	grass	grass litter - mostly decomposed	Lab	Meerdink et al. (2019)
OPE3_corn_P	GV	crop	<i>Zea mays</i> (corn) canopy spectrum, assessed for canopy closure using field data	Field	N/A
COFIV0702	GV	crop	<i>Gossypium hirsutum</i> (cotton) canopy spectrum, assessed for canopy closure using photography	Field	Marshall and Thenkabail (2014)
RIWIL0101	GV	crop	<i>Oryza sativa</i> (rice) canopy spectrum, assessed for canopy closure using photography	Field	Marshall and Thenkabail (2014)
SERC_decid_529_2941	GV	tree	broadleaf deciduous tree canopy spectrum from 1 m NEON imaging spectrometer (IS) pixel, scene NEON_D02_SERC_DP1_20210811_155341, interpolated to 1 nm	Image	NEON (2022)
SERC_soy_685_7088	GV	crop	soybean canopy spectrum from 1 m NEON IS pixel, scene NEON_D02_SERC_DP1_20210811_155341, interpolated to 1 nm	Image	NEON (2022)
WREF_conif_497_6428	GV	tree	needleleaf evergreen tree canopy spectrum from 1 m NEON IS pixel, scene NEON_D16_WREF_DP1_20210723_194155, interpolated to 1 nm	Image	NEON (2022)

The selected NPV endmembers (Fig. 2A) demonstrate variability in lignocellulose absorption. While several endmembers have local minima located near the 2100 nm reflectance minimum traditionally used for CAI (Nagler et al., 2000), other endmembers have minima at shorter or longer wavelengths dependent on cellulose and lignin content. VH358 and COP\_20160526\_5-40-W have local minima at wavelengths close to or slightly shorter than 2100 nm, indicating higher cellulose content relative to lignin (Kokaly et al., 2009). Conversely, a broadleaf deciduous leaf stack spectrum LL-1-87y has a local minimum near 2140 nm, indicating a lower cellulose-to-lignin ratio. Cellulose-to-lignin ratio also impacts the shape and position of the 2300 nm absorption feature in vegetation spectra (Kokaly et al., 2009). All spectra exhibit a local minimum close to 2275 nm, but inferred high-ratio spectra have a single, broader absorption feature at wavelengths longer than 2300 nm,

while inferred low ratio spectra (e.g., LL-1-87y and LL-2-89z) show two narrower absorption features at wavelengths longer than 2300 nm.

The GV spectral library (Fig. 2B) was less extensive. Field spectra of mature corn, cotton, and rice canopies with complete canopy closure were selected as endmembers (Table 1). Obtaining relatively “pure” GV spectra for broadleaf deciduous and needleleaf evergreen tree canopies proved more challenging due to tree height and difficulty ascertaining GV purity. Instead, pixel spectra were selected from National Ecological Observatory Network (NEON) airborne imaging spectrometer data capturing a leaf-on deciduous tree canopy, coniferous tree canopy, and mature soybean field (NEON, 2022). 1 m pixels with the highest red-near infrared differences were selected for each vegetation type, and then were smoothed and spline interpolated from nominal 5 nm spectral resolution to match the 1 nm sampling of the field- and lab-sourced

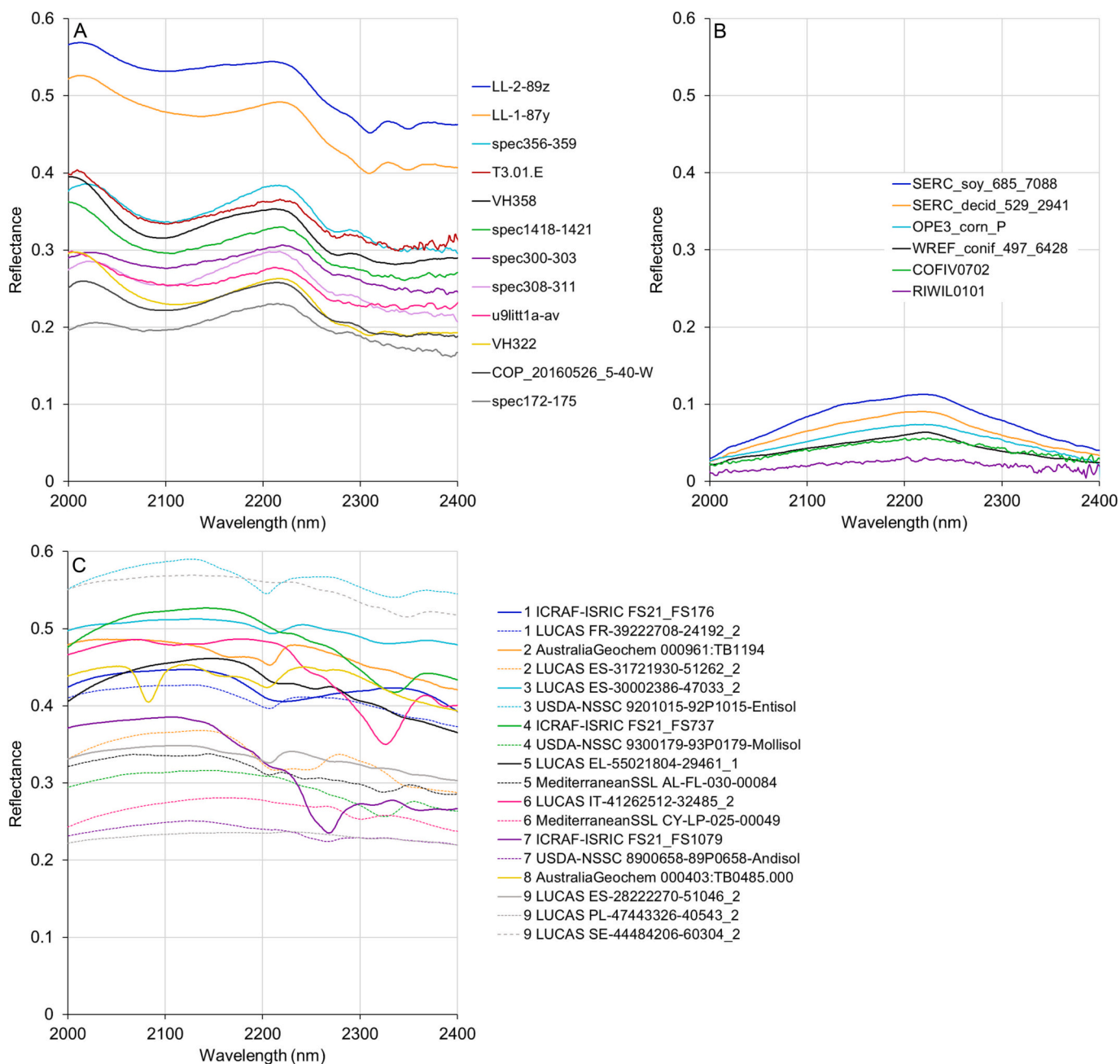


Fig. 2. A) NPV endmember spectra. The legend at right provides spectrum names in order of reflectance at 2200 nm. B) GV endmember spectra. The legend (inset) provides spectrum names in order of reflectance at 2200 nm. C) A subset of soil spectra representing the nine soil spectral classes. The legend (at right) provides spectrum names in order of soil class, indicated by the number before the soil spectrum name.

endmembers. GV endmembers were much darker in the SWIR2 region than NPV and soil endmembers (Fig. 2), with a shape dominated by canopy water absorption (Asner and Lobell, 2000).

The soils spectral library (Fig. 2C) was assembled in an effort to capture global variability in soils by distilling approximately 48,300 surface horizon spectra from six source soil spectral libraries into 228 endmembers representing nine spectral classes. The source soil spectral libraries included:

- World Agroforestry Center-International Soil Reference and Information Centre (ICRAF-ISRIC) globally distributed soil spectral library ( $n = 754$ ) (Viscarra Rossel et al., 2016; World Agroforestry (ICRAF) and International Soil Reference and Information Centre (ISRIC), 2021)
- Mediterranean regional soil spectral library ( $n = 1751$ ) (GeoCradle, 2021)
- European Land Use and Coverage Area frame Survey (LUCAS) soil spectral library ( $n = 43,560$  which includes duplicate spectral measurements of each sample) (Orgiazzi et al., 2018)
- Australian National Geochemistry Survey soil spectral library ( $n = 1308$ ) (Lau et al., 2019)
- United States Department of Agriculture (USDA) National Soil Survey Center (NSSC) soil spectral library, which includes US and global soils ( $n = 854$ ) (Brown et al., 2006)
- Brazilian Soil Spectral Library (BSSL) (selected subset  $n = 100$ ) (Dematté et al., 2019)

The MICA module of the US Geological Survey PRISM (Processing Routines in IDL for Spectroscopic Measurements) software (Kokaly, 2011) was used to identify spectral features associated with SWIR2 mineral absorptions in the source libraries. MICA matches analyzed spectra to a set of reference spectra using linear continuum removal, least-squares linear regression, and threshold constraints. Based on MICA reference libraries used for mineral identification in prior research (Graham et al., 2018; Moskowitz et al., 2016; Reynolds et al., 2014, 2020), we created a reference library containing 115 mineral spectra with SWIR2 absorption features, plus 21 spectra of other common surface materials (e.g., vegetation, water, snow). MICA matched each spectrum in the source libraries to a spectrally dominant material from the reference library.

A stratified random sampling was used to select a representative subset of 228 soil endmembers. This number of endmembers was selected to preserve the relative abundance of 60 MICA-identified mineral types identified in the source soil spectral libraries, while also limiting the total number of NPV-GV-soil endmember combinations. The relative abundance of minerals in the subset was skewed lower for the most abundant mineral types; this was necessary in order to keep the total number of spectra in the subset to a computationally manageable size and yet have at least one representative spectrum for the mineral types that were less frequently detected in source data. Temperate latitude soils are likely overrepresented in the soils spectral library compared to their global distribution, due to their source spectral libraries lacking true global representation (Viscarra Rossel et al., 2016).

The 228 soil endmembers were assigned to nine soil spectral classes defined by the wavelength positions and dominance of absorption features within different portions of the SWIR2 region (Table 2). Fig. 2C provides representative examples of endmembers from each soil spectral class. For most classes, absorption features are limited to wavelengths longer than 2170 nm (Fig. 2C). Soil spectral class 8 is the notable exception. Class 8 is comprised of a single endmember (Table 2), indicating its uniqueness and rarity within the source spectral libraries. This endmember has an unusual absorption feature centered near 2070 nm caused by the mineral topaz, and is the only endmember with prominent spectral features close to the 2100 nm lignocellulose absorption feature (Fig. 2B, C). Soil spectral class 9 was comprised of weak or unmatched mineral absorption features. The top-most dashed gray line in Fig. 2C

**Table 2**  
Soil spectral classes.

Soil Spectral Class	Dominant Spectral Feature	Number of Endmembers	Description of SWIR-Absorbing Minerals in Representative Soils
1	2200 nm	64	mostly montmorillonite, some kaolinite + smectite mixes, with a few gypsum and hydrated silica dominated spectra
2	2200 nm & 2300 nm	88	white mica (muscovite/illite), kaolinite, kaolinite + white mica(muscovite/illite) mixes, chlorite + muscovite and white mica (muscovite/illite) + carbonate (calcite/dolomite)
3	2300 nm & 2200 nm	20	carbonate (calcite/dolomite) mixtures with montmorillonite or white mica (muscovite/illite)
4	2300 nm	19	carbonate (calcite/dolomite/ aragonite), and a few others (vermiculite, nontronite, saponite)
5	2200 nm 2250 nm & 2300 nm	11	chlorite + white mica (muscovite/illite) or biotite group mineral + white mica (muscovite/illite) or amphibole group mineral + white mica (muscovite/illite) or kaolinite + muscovite or carbonate + smectite/white mica or biotite group mineral + white mica (muscovite/illite) or amphibole group mineral + white mica (muscovite/illite)
6	2300 nm & 2250 nm	6	chlorite/epidote or biotite group mineral + white mica (muscovite/illite) or amphibole group mineral + white mica (muscovite/illite) or other smectite group mineral (hectorite) or serpentine group mineral
7	2270 nm	4	gibbsite
8	2070 nm 2200 nm & 2300 nm	1	topaz bearing
9	Weak or Unmatched Features	15	relatively featureless, or may have features that are too weak to conclusively identify mineralogy, or cannot be matched to mineralogy

(LUCAS SE-44484206-60304\_2) indicates an endmember with a shallow, unmatched absorption feature with a minimum near 2350 nm. Another class 9 endmember in Fig. 2C, LUCAS PL-47443326-40543\_2, has no apparent absorption features.

The seven remaining soil spectral classes have absorption features that overlap with or are adjacent to the 2300 nm lignocellulose absorption feature (Fig. 2B, C). Class 1 spectra exhibit a mineral absorption feature near 2200 nm. Class 2 spectra have a 2200 nm absorption feature and a relatively weak absorption feature near 2300 nm, while class 3 spectra have a stronger 2300 nm feature relative to their 2200 nm feature. Class 4 spectra exhibit strong features near 2300 nm. Class 5 spectra exhibit multiple features near 2200, 2250, and 2300 nm. Class 6 spectra exhibit absorption features near 2250 and 2300 nm, and Class 7 spectra have absorption near 2270 nm.

### 2.1.2. Creating synthetic mixtures

Twelve NPV endmembers, 228 soil endmembers, and six GV endmembers allowed for 16,416 unique three-endmember combinations. To test the ability of different indices to estimate NPV fractional cover, random linear mixtures of reflectance endmembers were created using a

Dirichlet function, which at  $\alpha = 1$  provided a uniform distribution of mixtures across the three-endmember mixing space. Non-linear reflectance of vegetation-soil mixing due to multiple scattering is a well-known issue (Borel and Gerstl, 1994). Somers et al. (2009) found a 0.03–0.07 RMSE in the SWIR2 spectral region when comparing modeled and measured mixtures of soil, tree, and weed fractional cover. To reduce the potential error associated with a wide range of GV non-linear mixing and simultaneously reduce representation of strong liquid water absorption in mixtures associated with high GV cover, mixtures with >50% GV cover were excluded from further analysis. More than 1.05 million random mixtures were used in evaluating potential fractional NPV cover indices.

Mixtures created from lab and field endmembers have reduced structural shadowing and relatively low water content, resulting in higher SWIR2 reflectance than satellite-measured spectra. To produce a more realistic SWIR2 reflectance distribution, each mixture was multiplied by a random darkening factor. Landsat 8 Operational Line Imager (OLI) SWIR2 band data were used to set the range of the darkening factor. The median SWIR2 reflectance for every National Land Cover Database (NLCD) cropland, rangeland, and natural grassland pixel (Jin et al., 2019) within the continuous US between 15 April and 15 July 2016 were used to create a reference distribution. This time period captured a mix of dormant-period NPV and high crop residue conditions in spring, as well as landscape green-up into summer, culminating in a representative range of fractional cover conditions across multiple climate zones. Mixtures were convolved using Landsat 8 OLI relative spectral response to compare distributions of reflectance values to the distribution from actual Landsat data (Fig. S1). A darkening factor created using a uniform random distribution bounded by [0.25, 1] was empirically found to approximate the reference distribution. This random darkening factor was applied to all mixture spectra, uniformly across all SWIR2 wavelengths.

## 2.2. Index comparison

### 2.2.1. Resampling mixtures and adding sensor noise

Darkened synthetic mixtures were convolved from 1 nm sampling to hyperspectral bandpasses and multispectral bandwidths. Hyperspectral and multispectral band centers were separated by 5 nm. Hyperspectral bandpass functions used a Gaussian relative spectral response with a 10 nm full width-half maximum (FWHM) to approximate imaging spectrometer band relative spectral response (Green et al., 1998).

A uniform “boxcar” relative spectral response was used for resampling to multispectral bands (Hively et al., 2021; Lamb et al., 2022). A boxcar function represents a reasonable simplification of filter-based multispectral instrument relative spectral response; more detailed hypothetical response functions were examined and provided similar results. Hively et al. (2021) found that 30, 40, and 50 nm bandwidths produced similar error when used in multispectral indices for NPV cover estimation. However, they found that the reference band for 2100 nm lignocellulose absorption indices can be impacted by atmospheric carbon dioxide and water vapor absorption, and determined that a 10–30 nm bandwidth for a proposed band at 2040 nm would be well-positioned within the width of an atmospheric transmission window. Based on these prior findings, our multispectral analysis used a 40 nm bandwidth for multispectral bands at or longer than 2100 nm and used radiative transfer modeling to refine the bandwidth of multispectral bands shorter than 2100 nm. The MODTRAN6 radiative transfer model (Berk et al., 2014) was used to simulate atmospheric transmittance within the SWIR2 spectral region. Based on an assumed need for future sensors to be able to measure NPV cover through fall senescence in temperate climates, radiative transfer modeling assumed a 60° solar zenith angle that corresponds with a late-morning overpass at 45°N latitude approximately one month after the autumnal equinox. A nadir view zenith angle was assumed. To model transmittance for “dry” and “moist” atmospheres, column water vapor values of 1 and 4 g cm<sup>-2</sup> were

used. Radiative transfer modeling demonstrated that, once a band center tolerance of  $\pm 2$  nm was taken into account, the maximum allowable bandwidth for a reference band between 2000 and 2100 nm is 25 nm (Fig. 3). Thus, a 25 nm bandwidth was used for multispectral bands between 2000 and 2100 nm. Note that mean atmospheric transmittance, averaged across a 25 nm bandwidth, peaks at 2038 nm (Fig. 3).

After mixtures were convolved to hyperspectral and multispectral bands, simulated sensor noise was added to all reflectance values. A range of signal-to-noise ratios (SNRs) was applied to reflectance values used to calculate the indices described in Section 2.2.2. A 130:1 SNR was selected as representing maximum desirable sensor noise under reference conditions (60° solar zenith angle and 12% surface reflectance corresponding to the 25th percentile of the adjusted reflectance distribution at 2100 nm). Noise was added to reflectance values by generating random Gaussian numbers with a mean of zero and standard deviation of one, scaling by 1/130 multiplied by reflectance, and then adding a scaled random noise value to the reflectance value for each band.

### 2.2.2. Spectral indices

Two- and three-band versions of difference (DI), ratio (RI), and normalized difference indices (NDI) were calculated from the spectrally resampled hyperspectral and multispectral mixtures and regressed against the fractional NPV cover associated with each mixture (Table 3). Two-band indices used bands centered at wavelengths  $\lambda_a$  and  $\lambda_b$ , where  $a$  and  $b$  indicate distinct band centers within the 2000–2400 nm range. Three-band indices used bands centered at wavelengths  $\lambda_x$ ,  $\lambda_y$  and  $\lambda_z$ , where  $x$ ,  $y$ , and  $z$  indicate distinct band centers within the 2000–2400 nm range.

Two- and three-band indices were calculated for all possible combinations of bands, within the following constraints:

- 1) band combinations could not have overlapping FWHM/bandwidth;
- 2) for two-band indices,  $\lambda_a < \lambda_b$ ; and
- 3) for three-band indices,  $\lambda_x < \lambda_y < \lambda_z$ .

Ignoring the second and third constraints was tested but did not meaningfully impact results, so we kept these constraints in place to simplify index descriptions.

For 2100 and 2300 nm lignocellulose absorption features, either  $a$  or  $b$  can serve as a reference band while the remaining band is within the absorption feature. For three-band indices under the third constraint,  $x$  and  $z$  serve as reference bands. These reference bands can straddle the absorption feature, placing  $y$  within the feature, effectively creating an absorption index. Alternatively, the two reference bands can reside within separate lignocellulose absorptions, placing  $y$  on the peak between the absorptions and effectively creating a peak index.  $y$  will be referred to as the “feature band”, and can indicate either depth of lignocellulose absorption or height of the peak between absorptions.

Neither RI nor NDI indices are reciprocal (e.g., the relationship between NPV cover and  $(\lambda_a - \lambda_b)/(\lambda_a + \lambda_b)$  is not identical to the relationship between NPV cover and  $(\lambda_b - \lambda_a)/(\lambda_b + \lambda_a)$ ). Reciprocal forms for RI and NDI were tested, but again did not meaningfully impact results, so only the index forms shown in Table 3 were used.

RI3 and NDI3 perform best for spectral features that are symmetrical, since  $\rho_{\lambda_x}$  and  $\rho_{\lambda_z}$  are given equal weighting in index equations. If a spectral feature is asymmetrical, equal weighting used for the two reference bands ( $x$ ,  $z$ ) will not accurately represent the linear reflectance trend at the wavelength of band  $y$ . To improve performance over three-band indices that assume symmetry, the continuum interpolated band ratio (CIBR) was tested (Eq. 7). CIBR is a differential absorption technique that weights reference bands based on their wavelength to measure spectral feature depth or height (Dennison, 2006; Green et al., 1989). This index form divides the reflectance of the feature band by the reflectance of two reference bands interpolated to the wavelength of the feature band, and is thus well-suited to asymmetrical spectral features. CIBR depends on calculation of weights  $w_x$  and  $w_z$ , described in eqs. 8

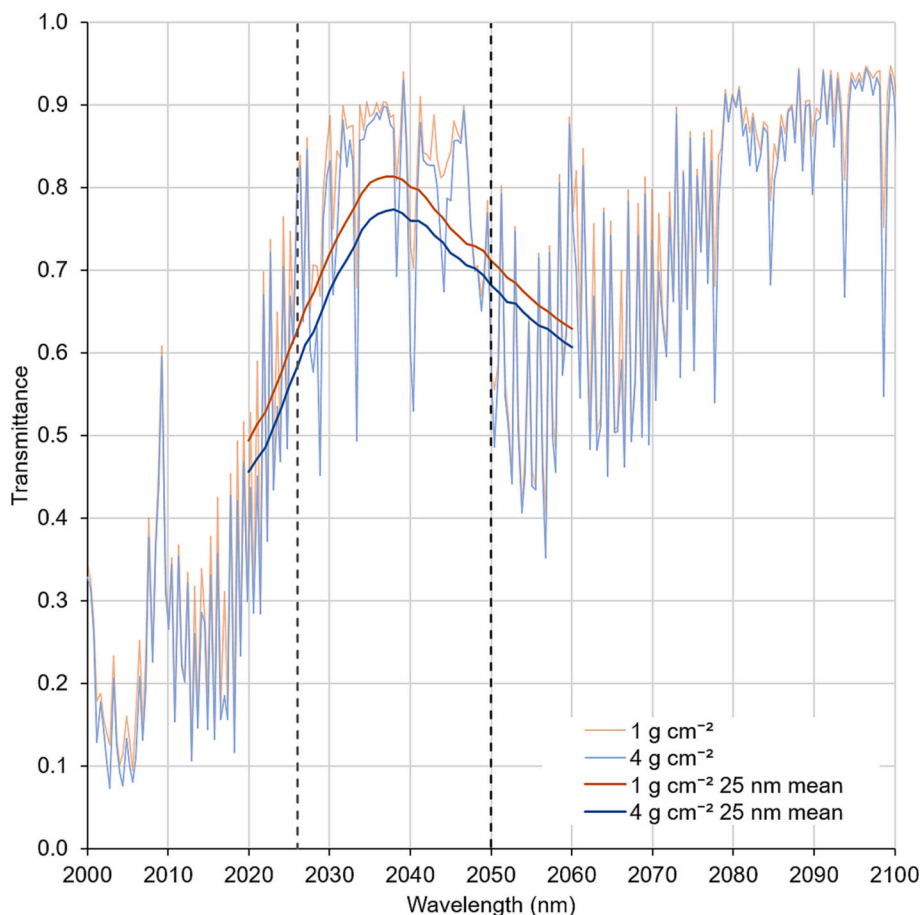


Fig. 3. Atmospheric transmittance modeled by MODTRAN for a 60° solar zenith angle and “dry” (1 g cm<sup>-2</sup>) and “moist” (4 g cm<sup>-2</sup>) atmospheres. Lightly shaded lines show transmittance at 1 cm<sup>-1</sup> resolution. Darkly shaded lines show transmittance averaged across 25 nm bandwidth, at a 1 nm interval. Dashed lines indicate a 25 nm bandwidth centered at 2038 nm.

Table 3

Index forms used to estimate fractional NPV cover.  $\rho$  signifies reflectance, with wavelength ( $\lambda$ ) subscripts defined in Section 2.2.2. CIBR uses two weights ( $w$ ) applied to reflectances of the x and z bands.

Name	Two-band equation	Three-band equation
difference index (DI)	DI2 = $\rho_{\lambda_a} - \rho_{\lambda_b}$ (1)	DI3 = $2\rho_{\lambda_y} - (\rho_{\lambda_x} + \rho_{\lambda_z})$ (2)
ratio index (RI)	RI2 = $\frac{\rho_{\lambda_a}}{\rho_{\lambda_b}}$ (3)	RI3 = $\frac{2\rho_{\lambda_y}}{\rho_{\lambda_x} + \rho_{\lambda_z}}$ (4)
normalized difference index (NDI)	NDI2 = $\frac{\rho_{\lambda_a} - \rho_{\lambda_b}}{\rho_{\lambda_a} + \rho_{\lambda_b}}$ (5)	NDI3 = $\frac{(\rho_{\lambda_x} + \rho_{\lambda_z}) - 2\rho_{\lambda_y}}{(\rho_{\lambda_x} + \rho_{\lambda_z}) + 2\rho_{\lambda_y}}$ (6)
continuum interpolated band ratio (CIBR)		CIBR = $\frac{\rho_{\lambda_y}}{(w_x \rho_{\lambda_x} + w_z \rho_{\lambda_z})}$ (7) where: $w_x = \frac{\lambda_z - \lambda_y}{\lambda_z - \lambda_x}$ (8) $w_z = \frac{\lambda_y - \lambda_x}{\lambda_z - \lambda_x}$ (9)

and 9. If  $\lambda_x - \lambda_y = \lambda_z - \lambda_y$ , weights will be equal and CIBR will produce index values identical to those from RI3. The CIBR form is consistent with previous spectroscopic studies that have applied linear continuum removal and feature depth calculations to estimate abundances of plant biochemicals (Kokaly and Clark, 1999; Kokaly and Skidmore, 2015).

Linear regression used each index value derived from a band combination as the independent variable, with fractional NPV cover as the dependent variable. Regression coefficients were calculated using 70% of the simulated mixtures as training data. The remaining 30% of

simulated mixtures were reserved as testing data and used to determine model fit and error, calculated as R<sup>2</sup> and RMSE, respectively. Two candidate indices, both CIBRs, were identified based on lowest RMSE values within their respective parts of the SWIR2 spectral region and used for sensitivity analyses.

### 2.3. Sensitivity analyses

#### 2.3.1. Modeling uncertainty due to reflectance retrieval

Retrieving reflectance from at-sensor radiance contributes to measurement uncertainty, and ultimately to error in NPV cover estimation. Reflectance retrieval uncertainty for candidate multispectral indices was examined by using radiative transfer modeling in 6S (Vermote et al., 1997). Previous reference conditions representing a late morning overpass at 45° N approximately one month after the autumnal equinox (60° solar zenith angle) and 25th percentile reflectance (12%) were used in modeling. Reflectance retrieval uncertainty was calculated using a sensitivity analysis where column water vapor uncertainty was assumed to be 0.2 g cm<sup>-2</sup> based on Makarau et al. (2017) and column CO<sub>2</sub> and CH<sub>4</sub> uncertainty were assumed to be +/- 2%. Both a 1 g cm<sup>-2</sup> “dry” atmosphere and a 4 g cm<sup>-2</sup> “moist” atmosphere were modeled to reveal how sensitivity to column water vapor impacted reflectance uncertainty and error in estimated NPV cover. Additional modeling in 6S was used to reveal sensitivity of reflectance uncertainty to a hypothetical uncharacterized post-launch +/- 2.5 nm shift in band center wavelength. 130:1 sensor SNR was included in all reflectance uncertainty estimates, which were applied to synthetic mixtures as a Gaussian-distributed random error.

After including reflectance uncertainty, candidate multispectral indices were tested on subsets of the simulated mixtures. A “global” model using all soil spectral classes was compared to “local” models specific to each soil class. Model error for the global model was also assessed within 10% intervals of GV and soil cover.

### 2.3.2. Sensitivity to soil and NPV moisture

Endmembers from the soils spectral library represent dry soils, and candidate index performance may be impacted by the effects of soil moisture on mixture reflectance (Daughtry and Hunt, 2008; Quemada and Daughtry, 2016). To test the impacts of soil and NPV relative water content (RWC) on NPV cover estimation error, we applied candidate indices to spectra collected during a field experiment by Quemada and Daughtry (2016). In this experiment, maize residue was distributed over bare soil to vary NPV cover. Moisture was manipulated during the experiment, and both soil and NPV RWC were measured along with NPV cover within the spectrometer field of view.

Candidate multispectral indices were calculated for 410 field spectra, and then used as the independent variable in linear regressions with fractional NPV cover as the dependent variable. A 70%–30% random train/test split was used. Spectra were subset by total RWC, varying ranges in maximum RWC starting with 0–0.2 (i.e., relatively dry spectra) and increasing to 0–1.0 (i.e., full range in RWC). Daughtry and Hunt (2008) and Quemada and Daughtry (2016) demonstrated that error in CAI estimation of NPV cover could be reduced by adding a water ratio index based on the reflectance of the two reference bands to a multiple linear regression model. This water ratio index represents moisture impacts on soil and NPV reflectance. Using multiple linear regression, we tested applying similar water ratio indices based on candidate NPV index bands to examine improvement in RMSE across ranges in RWC. Water ratio indices were used in addition to candidate NPV indices as independent variables.

### 2.3.3. Continuity analysis

Candidate multispectral indices present options for SWIR2 bands that may produce biased reflectance values when compared against reflectance time series of previous Landsat SWIR2 bands. Heritage Landsat SWIR2 bands have centers ranging from 2200 nm (Landsat 8 and 9 OLI) to 2220 nm (Landsat 7 Enhanced Thematic Mapper+), and bandwidths ranging from 187 nm (Landsat 8 OLI) to 270 nm (Landsat 4 and 5 TM) (Goward et al., 2001; Masek et al., 2020; Mika, 1997). To assess how using candidate multispectral index band centers for Landsat Next might impact reflectance time series, a reflectance scene from the Earth Surface Mineral Dust Source Investigation (EMIT) imaging spectrometer (Green and Thompson, 2020) was used to simulate candidate band and Landsat 8 OLI SWIR2 band reflectances. The EMIT imaging spectrometer has 285 bands with band centers spanning 381–2493 nm and FWHM ranging from 8.4 to 8.8 nm. The EMIT surface reflectance product has an approximate 60 m spatial resolution.

EMIT\_L2A\_RFL\_001\_20220813T232355\_2222515\_004 is a diverse scene extending approximately 81 km by 82 km and containing the urban centers of Sacramento and Stockton, California, USA as well as large, surrounding agricultural and grassland areas. This scene was spectrally resampled using the relative spectral response of the Landsat 8 OLI SWIR2 band and boxcar functions for candidate index bands. 100,000 pixels were randomly sampled from the scene, and then candidate index band reflectances were regressed against simulated Landsat 8 OLI SWIR2 reflectance.  $R^2$  and RMSE for this regression were used to evaluate how well proposed index bands approximate heritage reflectance, and residual reflectance was calculated for each scene pixel. In addition, multiple linear regression was used to assess how ensembles of three index bands were able to approximate simulated Landsat 8 OLI SWIR2 band reflectance.

### 2.3.4. Estimated NPV cover images

To provide a qualitative comparison of index performance, bands

simulated from EMIT scene EMIT\_L2A\_RFL\_001\_20220813T232355\_2222515\_004 were used to calculate candidate multispectral indices. Linear regression slope and intercept from the synthetic mixture training data were used to convert scene index values to estimated fractional NPV cover.

## 3. Results

We provide results for the index comparison in separate sections for hyperspectral (Section 3.1) and multispectral (Section 3.2) analyses. The sections that follow (3.3–3.7) describe results from the sensitivity analyses.

### 3.1. Hyperspectral indices

Linear regressions between hyperspectral indices computed using simulated imaging spectrometer data (10 nm bandwidth, 5 nm band center spacing) and fractional NPV cover were evaluated using test dataset  $R^2$  and RMSE for 3160 two-band combinations and 79,079 three-band combinations. To provide an easily interpretable graphical representation of RMSE trends, the lowest RMSE at each wavelength was plotted for bands  $a$  and  $b$  (two-band indices) or  $x$ ,  $y$ , and  $z$  (three-band indices) in Fig. 4. Two-band index error was generally higher than three-band index error. Among two-band indices, NDI2 provided similar, but slightly lower RMSE compared to RI2. Both ratio indices distinctly improved RMSE compared to DI2. Minimum RMSE occurred at the same wavelengths for all three two-band indices, with  $\lambda_a$  at 2030 nm and  $\lambda_b$  at 2095 nm. For NDI2, this band combination produced a 0.1489 RMSE and 0.613  $R^2$ . However, 2030 nm might be an impractical band center choice due to reduced atmospheric transmittance at this wavelength (Fig. 3).

A local minimum for NDI2 occurred for  $\lambda_a$  at 2220 nm and  $\lambda_b$  at 2270 nm (RMSE = 0.1588,  $R^2$  = 0.559). This two-band index is very similar to SINDRI, which uses the NDI2 form with  $\lambda_a$  at 2210 nm and  $\lambda_b$  at 2260 nm (Serbin et al., 2009b). By better accounting for variability in soil and NPV spectral shape, the NDI2 with  $\lambda_a$  at 2220 nm and  $\lambda_b$  at 2270 nm provided moderate improvement in error over the two-band combination used for SINDRI (RMSE = 0.1659,  $R^2$  = 0.519).

For three-band hyperspectral indices, RI3 and NDI3 again had very similar RMSE, with both outperforming DI3 (Fig. 4). The minimum RMSE of three-band combinations for RI3 and NDI3 had nearly identical 0.675  $R^2$  values, but RI3 produced a slightly lower RMSE (0.1363 for RI3, 0.1364 for NDI3). Minimum RMSE for RI3 occurred for  $\lambda_x$  at 2025 nm,  $\lambda_y$  at 2115 nm, and  $\lambda_z$  at 2190 nm. Minimum RMSE for NDI3 occurred for  $\lambda_x$  at 2025 nm,  $\lambda_y$  at 2125 nm, and  $\lambda_z$  at 2195 nm. For both of these indices, the 2025 nm band center is problematic because of reduced atmospheric transmittance due to carbon dioxide absorption (Fig. 3). CAI, with a DI3 index form, had high RMSE (0.1599) in comparison to ratio indices.

Since the CIBR index form can better accommodate the asymmetrical shape of the 2100 nm lignocellulose absorption feature, it improved minimum RMSE and shifted band wavelengths in comparison to the symmetrical three-band indices. A RMSE minimum of 0.1355 ( $R^2$  = 0.679) for CIBR occurred for  $\lambda_x$  at 2030 nm,  $\lambda_y$  at 2110 nm, and  $\lambda_z$  at 2215 nm. While minimum RMSE and  $R^2$  were similar for CIBR, RI3, and NDI3, CIBR's weighted index form provided four important advantages, as can be seen in Fig. 4:

- 1) slightly reduced RMSE in comparison to RI3 and NDI3;
- 2) the first reference band ( $\lambda_x$ ) minimum RMSE shifts to longer wavelengths and the minimum RMSE valley broadens, allowing this band center to be placed at a wavelength with higher atmospheric transmittance;
- 3) the feature band ( $\lambda_y$ ) minimum RMSE valley is broader and occurs closer to 2100 nm; and.

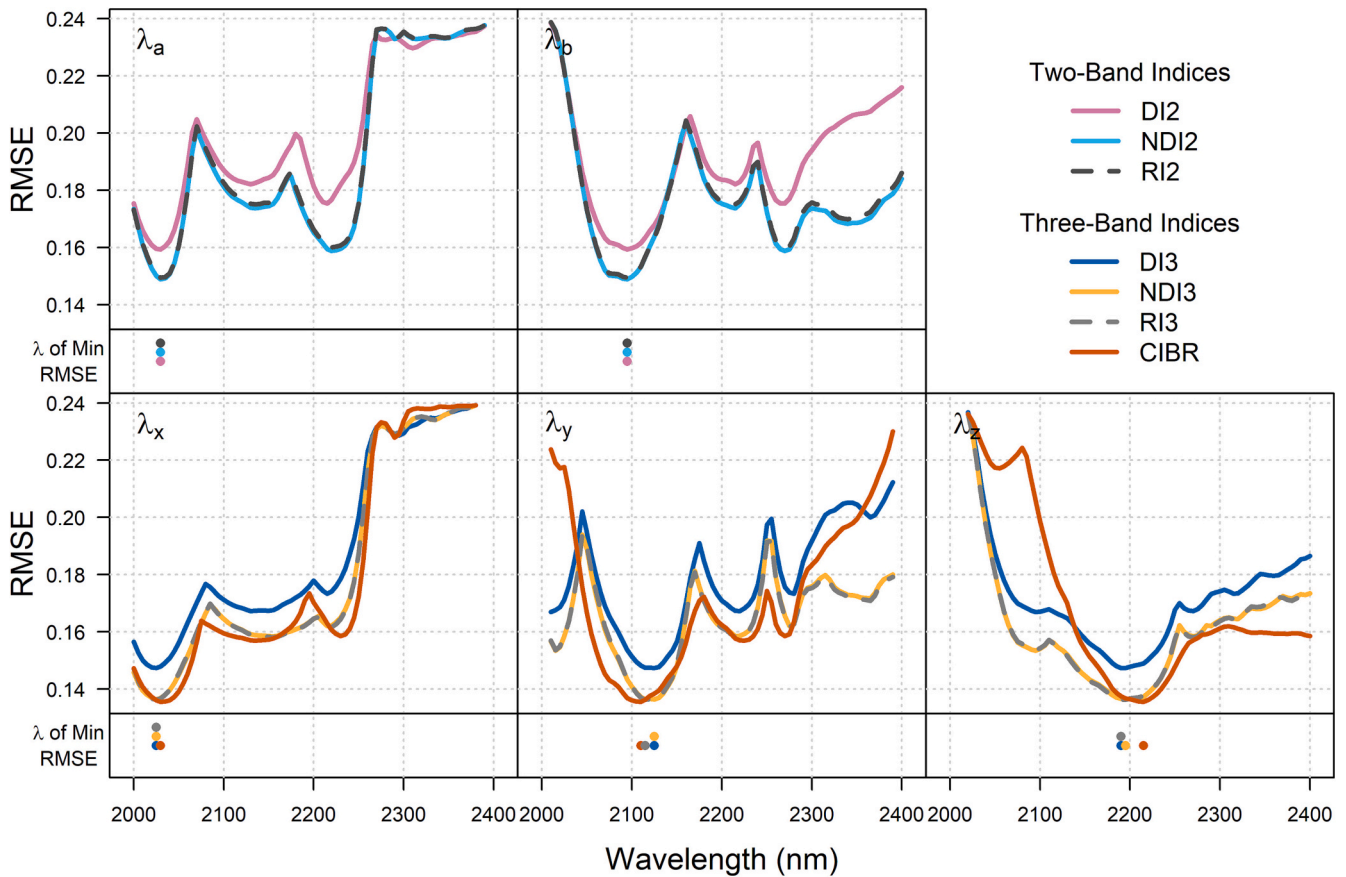


Fig. 4. Lowest root mean squared error (RMSE) for hyperspectral two- and three-band indices at each wavelength. Dots indicate the minimum RMSE band combinations for each index.

4) the third reference band ( $\lambda_z$ ) has its minimum RMSE at longer wavelengths, potentially improving continuity with heritage SWIR2 bands used by previous multispectral systems like Landsat OLI.

Because of the increased width of the  $\lambda_x$  reference band minimum RMSE valley, alternative CIBR bands with better atmospheric transmittance can be selected with minimal reductions in accuracy. For example,  $\lambda_x$  at 2035 nm,  $\lambda_y$  at 2110 nm, and  $\lambda_z$  at 2215 nm produced a 0.1357 RMSE and 0.678  $R^2$ , and  $\lambda_x$  at 2040 nm,  $\lambda_y$  at 2105 nm, and  $\lambda_z$  at 2215 nm produced a 0.1361 RMSE and 0.676  $R^2$ .

Additionally, a local minimum CIBR capturing the reflectance peak between 2100 and 2300 nm lignocellulose absorption occurred for  $\lambda_x$  at 2135 nm,  $\lambda_y$  at 2225 nm, and  $\lambda_z$  at 2265 nm, producing a 0.1570 RMSE and 0.569  $R^2$ . 2225 nm and 2265 nm are close to local minimum NDI2 wavelengths, and also close to wavelengths used for SINDRI. Remarkably, there appears to be only a minor benefit to adding a third band residing in the 2100 nm lignocellulose absorption feature. The local minimum three-band CIBR reduced RMSE by 0.0018 and improved  $R^2$  by 0.01 in comparison to the local minimum two-band NDI.

Two new CIBR indices were defined based on these results. The hyperspectral version of the Continuum Interpolated NPV Depth Index (CINDI) is based on the CIBR using band centers of 2035, 2110, and 2215 nm for  $\lambda_x$ ,  $\lambda_y$ , and  $\lambda_z$ , respectively. The equation for CINDI subtracts the CIBR from 1 to provide a “band depth” value that is positively correlated with fractional NPV cover:

$$CINDI_h = 1 - \left( \frac{\rho_{2110}}{0.583\rho_{2035} + 0.416\rho_{2215}} \right) \quad (10)$$

where the  $h$  subscript indicates hyperspectral bands based on simulation of imaging spectrometer data, reflectance subscripts indicate

wavelength in nm, and weights were calculated using eqs. 8 and 9 (in Table 3). CINDI can be thought of as a weighted, ratioed version of CAI that has been optimized for atmospheric transmittance and spectral variability in both NPV and soils.

The hyperspectral version of the Dual Absorption NPV Index (DANI) is based on the CIBR using 2135, 2225, and 2265 nm band centers, and is also positively correlated with fractional NPV cover:

$$DANI_h = \frac{\rho_{2225}}{0.3077\rho_{2135} + 0.6923\rho_{2265}} \quad (11)$$

where the  $h$  subscript on DANI indicates hyperspectral bands based on simulation of imaging spectrometer data, reflectance subscripts indicate wavelength in nm, and weights were calculated using eqs. 8 and 9 (in Table 3). DANI measures the height of the peak between the 2100 and 2300 nm lignocellulose absorption features (Fig. 5B), and is a weighted version of the “center peak ratio” index described by Lamb et al. (2022), optimized for spectral variability in both NPV and soils.

Fig. 5 provides illustrated examples of  $CINDI_h$  and  $DANI_h$  for endmembers from the NPV spectral library, with selected 10 nm hyperspectral index bands shown in dark gray. CINDI measures the depth of the 2100 nm lignocellulose absorption feature (Fig. 5A), while DANI measures the height of the peak between the 2100 and 2300 nm lignocellulose absorption features (Fig. 5B). Each plot shows the linearly interpolated reference reflectance for endmember VH358 as a green circle. CINDI’s use of weighting increases the measured depth of the absorption feature over an unweighted index, since the mean of the two reference bands would have a lower reflectance value in Fig. 5A. Similarly, DANI’s use of weighting increases the measured height of the peak, since the mean of the two reference bands would have a higher reflectance value in Fig. 5B.

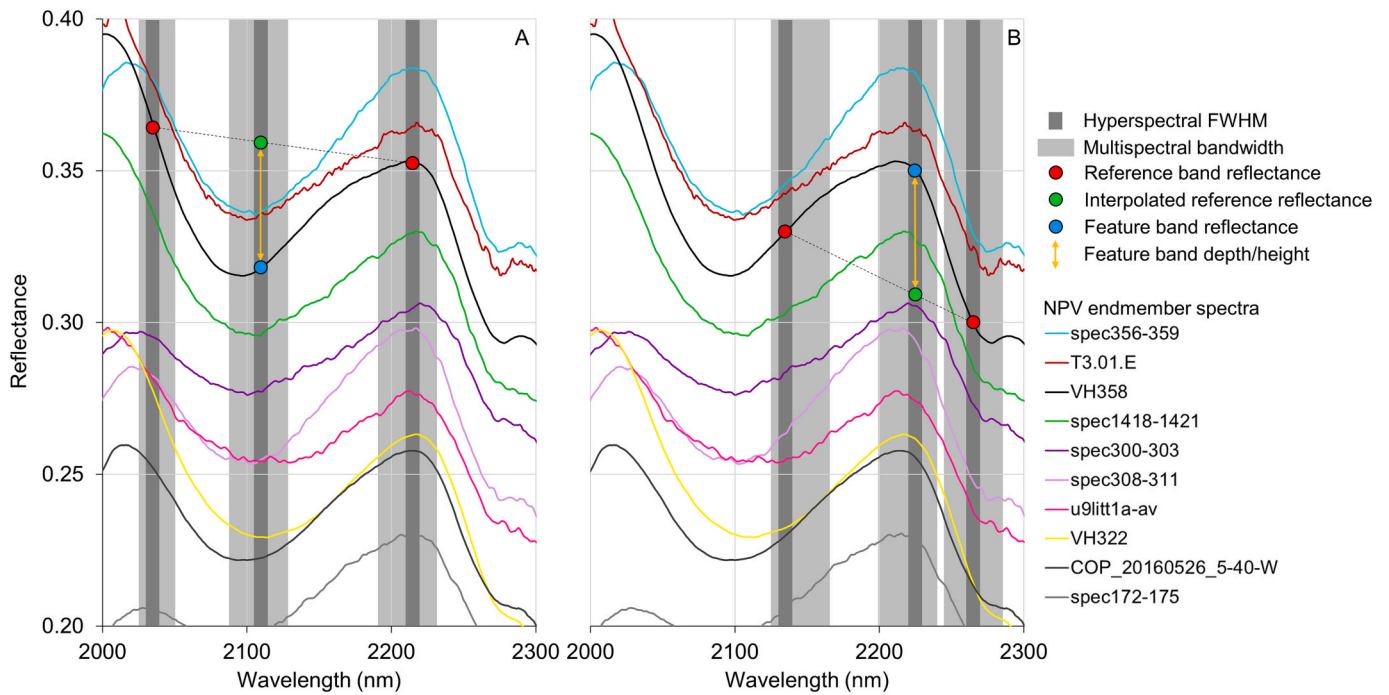


**Fig. 5.** Plots demonstrating hyperspectral (dark gray) and multispectral (light gray) bands for A) CINDI and B) DANI. A subset of the NPV endmembers from Fig. 2A are also shown. For each plot, endmember VH358 reference band, interpolated reference, and feature band reflectances for hyperspectral bands are shown as circles. The feature band depth (A) or height (B) for VH358 is indicated by the vertical orange line, and the dashed black line is the interpolated linear trend between reference bands.

CINDI<sub>h</sub>'s feature band ( $\lambda_y$ ) at 2110 nm is positioned near the center of local reflectance minima produced by varying cellulose-to-lignin ratio (Fig. 5A). CINDI<sub>h</sub>'s second reference band ( $\lambda_z$ ) at 2215 nm is well-aligned with the reflectance peak between the 2100 and 2300 nm lignocellulose absorption features. In contrast, DANI<sub>h</sub>'s feature band ( $\lambda_y$ ) at 2225 nm is shifted slightly to the right of this reflectance peak.

Scatterplots demonstrate linear relationships between predicted and observed NPV cover, with a tighter correlation for CINDI in comparison to DANI (Fig. 6, top row). As expected with an  $R^2$  and slope closer to one, CINDI has a smaller y-intercept than DANI. As would be expected with any linear regression model, both indices overpredict NPV cover at low fractions and underpredict NPV cover at high fractions.

### 3.2. Multispectral indices

Broadened bandwidths of simulated multispectral data increased the potential for overlapping bands and thus reduced the number of compared band combinations to 2701 for two-band indices and 47,905 for three-band indices. Broadened bandwidths had minor impacts on RMSE and wavelength positions of bands with minimum RMSE (Fig. S2). NDII was again the two-band index with the lowest error (RMSE = 0.1499,  $R^2 = 0.607$ ), using band centers of 2030 and 2090 nm. NDII had a local minimum error (RMSE = 0.1618,  $R^2 = 0.542$ ) using band centers of 2225 and 2270 nm.

CIBR again had the lowest RMSE values compared to the other three-band index forms. At 5 nm band center intervals, the lowest RMSE for estimating fractional NPV cover was found for band centers of  $\lambda_x$  at 2030 nm,  $\lambda_y$  at 2110 nm, and  $\lambda_z$  at 2210 nm (RMSE = 0.1364,  $R^2 = 0.675$ ). These band centers are close to optimal band centers for CINDI<sub>h</sub> (Eq. 10). Multispectral CINDI bands were further refined by fixing  $\lambda_x$  at 2038 nm to maximize atmospheric transmittance (Fig. 3) and examining band combinations at 1 nm interval. Rather than find the minimum RMSE for a single three-band combination among many similar combinations, we averaged RMSE across a tolerance of  $\pm 2$  nm for the 2038 nm  $\lambda_x$  band center and  $\pm 4$  nm for the  $\lambda_y$  and  $\lambda_z$  band centers.

These tolerances could accommodate manufacturing of filters for any future multispectral/superspectral sensors adopting these bands. A minimum average RMSE of 0.1371 was found for  $\lambda_x$  at 2038 nm,  $\lambda_y$  at 2108 nm, and  $\lambda_z$  at 2211 nm. These three bands were used for the multispectral version of CINDI, which assumes 25 nm bandwidth for band x and 40 nm bandwidth for bands y and z:

$$CINDI_m = 1 - \left( \frac{\rho_{2108}}{0.5954\rho_{2038} + 0.4046\rho_{2211}} \right) \quad (12)$$

where the  $m$  subscript on CINDI indicates bands based on simulation of a multispectral sensor, reflectance subscripts indicate wavelength in nm, and weights were calculated using eqs. 8 and 9 (in Table 3).

A local minimum error in CIBR RMSE placed band centers for  $\lambda_x$  at 2145 nm,  $\lambda_y$  at 2220 nm, and  $\lambda_z$  at 2265 nm (RMSE = 0.1589,  $R^2 = 0.558$ ). These three bands were used for the multispectral version of DANI, which assumes 40 nm bandwidths for all bands:

$$DANI_m = \frac{\rho_{2220}}{0.375\rho_{2145} + 0.625\rho_{2265}} \quad (13)$$

where the  $m$  subscript on DANI indicates bands based on simulation of a multispectral sensor, reflectance subscripts indicate wavelength in nm, and weights were calculated using eqs. 8 and 9 (in Table 3).

Light gray shading in Fig. 5 denotes bandwidths for multispectral CINDI and DANI bands. Shifting the first CINDI<sub>m</sub> reference band ( $\lambda_x$ ) to slightly longer wavelengths (2038 nm band center) was a practical choice to maximize atmospheric transmittance for the broader multispectral band; note that for hyperspectral CIBR results (Section 3.1), a band combination using 2040 nm for  $\lambda_x$  also had low error. The wavelength position of the DANI<sub>m</sub> feature band shifted to slightly shorter wavelength (by 5 nm) compared to DANI<sub>h</sub> in a way that better covers the range in peak positions between 2100 and 2300 nm lignocellulose absorption features. The first DANI<sub>m</sub> reference band shifted to longer wavelength in comparison to the corresponding DANI<sub>h</sub> band.

Scatterplots for the multispectral versions of CINDI and DANI are remarkably similar to scatterplots for the hyperspectral versions of the

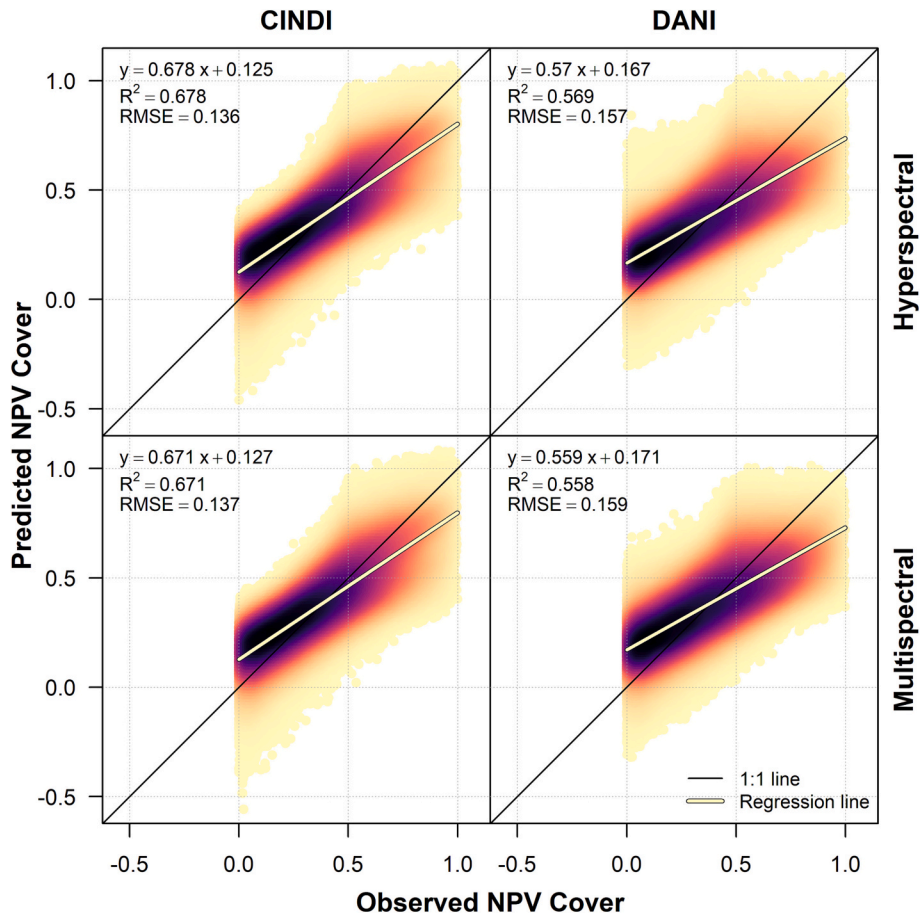


Fig. 6. Scatterplots showing relationships between predicted and observed fractional NPV cover for test data. Darker shades indicate higher sample density. The top row uses hyperspectral versions of CINDI (left) and DANI (right) indices as defined in Section 3.1. The bottom row uses multispectral versions of CINDI and DANI as defined in Section 3.2.

same indices (Fig. 6). Despite having broader bands, multispectral index  $R^2$ , intercept, and RMSE values are very close to those of their hyperspectral counterparts.

### 3.3. Multispectral reflectance uncertainty

Relative uncertainty in retrieved reflectance, which included 130

Table 4

Relative uncertainties (in percent) in retrieved reflectance for CINDI<sub>m</sub> and DANI<sub>m</sub> bands, as modeled under dry and moist atmospheres and with no band center shift and a 2.5 nm band center shift. 6S parameters for each model run are shown in italics.

	band	band center wavelength (nm)	bandwidth (nm)	Relative uncertainties (%)			
				<i>1</i>	<i>4</i>	<i>1</i>	<i>4</i>
<i>column water vapor (g cm<sup>-2</sup>)</i>				<i>1</i>	<i>4</i>	<i>1</i>	<i>4</i>
<i>band center shift (nm)</i>				<i>0</i>	<i>0</i>	<i>2.5</i>	<i>2.5</i>
CINDI <sub>m</sub>	<i>x</i>	2038	25	1.38	1.32	1.41	1.33
CINDI <sub>m</sub>	<i>y</i>	2108	40	1.05	0.97	1.22	1.17
CINDI <sub>m</sub>	<i>z</i>	2211	40	0.98	0.92	1.00	0.94
DANI <sub>m</sub>	<i>x</i>	2145	40	0.95	0.88	0.96	0.91
DANI <sub>m</sub>	<i>y</i>	2220	40	0.90	0.87	0.98	1.28
DANI <sub>m</sub>	<i>z</i>	2265	40	0.82	0.83	0.85	0.83

SNR, was approximately 1% (Table 4). Uncertainty was highest for the CINDI<sub>m</sub> *x* band, followed by the CINDI<sub>m</sub> *y* band. Both bands have higher sensitivity to uncertainty in water vapor and carbon dioxide. Uncertainty was generally lower for DANI<sub>m</sub> bands. Low column water vapor produced higher uncertainty than higher column water vapor, but differences were small. An uncharacterized  $\pm 2.5$  nm shift in band center had minor impacts on relative uncertainty. When reflectance uncertainty was taken into account, RMSE for CINDI<sub>m</sub>-modeled NPV cover increased to approximately 0.150 for the no band shift case (Table 5). RMSE for DANI<sub>m</sub>-modeled NPV cover increased to approximately 0.165 for the no band shift case.

### 3.4. CINDI<sub>m</sub> and DANI<sub>m</sub> sensitivity to soil spectral class and GV cover

With respect to mineral absorptions in the SWIR2 region, CINDI<sub>m</sub> was less sensitive to variability in soil spectral shape than DANI<sub>m</sub> (Fig. 7). Regardless of atmospheric moisture and bandshift, CINDI<sub>m</sub> had lower error in modeled NPV cover for all soil spectral classes with the exception of class 8, the class with a single spectrum for a topaz-bearing mineral. Soil spectral classes with absorption features close to 2250 and 2300 nm (classes 4, 6, and 7) produced much higher RMSE values when the DANI<sub>m</sub> global model was applied. These three high error soil classes represent carbonate, chlorite/epidote/biotite/serpentine group, and gibbsite minerals, respectively (Table 1). Using local models trained on each specific soil spectral class did reduce error, particularly for DANI<sub>m</sub>, but CINDI<sub>m</sub> still produced lower RMSE relative to DANI<sub>m</sub> for all classes with the exception of class 8.

With respect to fractional GV cover, CINDI<sub>m</sub> was broadly less

**Table 5**  
R<sup>2</sup> and RMSE for NPV cover modeled by CINDI<sub>m</sub> and DANI<sub>m</sub>, considering reflectance uncertainty and SNR.

Index	dry atmosphere				moist atmosphere			
	no band shift		2.5 nm band shift		no band shift		2.5 nm band shift	
CINDI <sub>m</sub>	0.600	0.1511	0.585	0.1539	0.607	0.1497	0.592	0.1526
DANI <sub>m</sub>	0.522	0.1652	0.517	0.1661	0.523	0.1651	0.498	0.1693

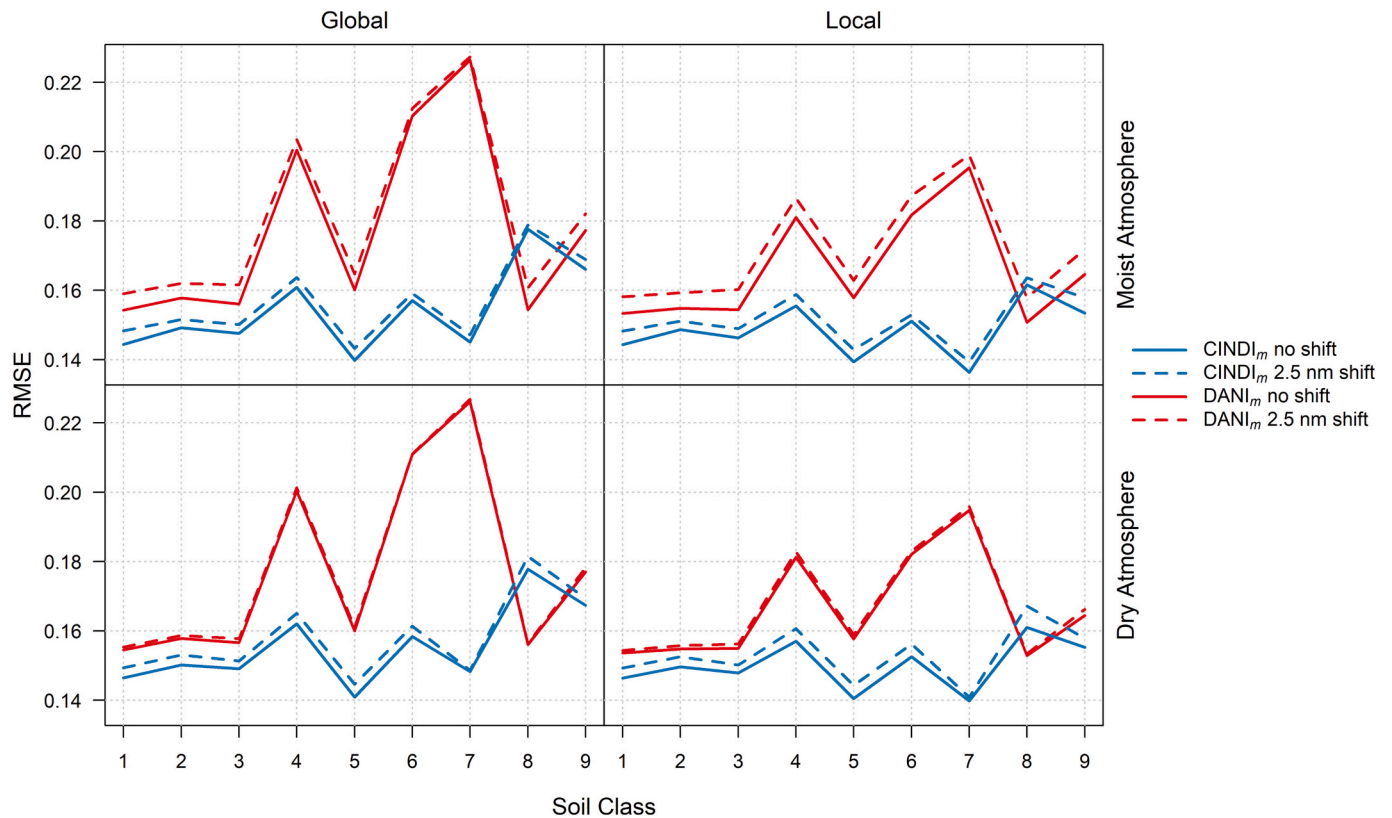


**Fig. 7.** Error in modeled fractional NPV cover based on reflectance uncertainty and SNR both with and without a modeled 2.5 nm band shift, for different soil spectral classes. Global models were trained on all soil classes and then applied to each class to assess error. Local models were trained on each soil class and then applied to the same class to assess error.

sensitive than DANI<sub>m</sub> (Fig. 8). For both indices, error in estimated NPV cover was lowest in the 20–40% GV cover range. RMSE was consistently below 0.14 within this range for CINDI<sub>m</sub>. DANI<sub>m</sub> RMSE was slightly lower than CINDI<sub>m</sub> RMSE for some cases at 20–30% GV cover, but in all other ranges CINDI<sub>m</sub> RMSE was lower. While error was similar in the 10–20% range, DANI<sub>m</sub> RMSE increased much more rapidly than CINDI<sub>m</sub> RMSE above 30% GV cover. For both GV cover (Fig. 8) and soil cover (Fig. S3), RMSE was highest in the 0–10% cover range with a general declining trend in error as GV or soil cover increased. A low GV or soil fraction enables a wider range in fraction of the two complementary endmembers, which in turn increases RMSE.

### 3.5. CINDI<sub>m</sub> and DANI<sub>m</sub> moisture sensitivity

RMSE for linear regression models broadly increased as the range in RWC increased in the Quemada and Daughtry (2016) dataset (Fig. 9), with lowest error generally occurring for the 0–20% RWC range. From 0 to 20% RWC, CINDI<sub>m</sub> had lower error in fractional NPV cover than DANI<sub>m</sub>. For wider RWC ranges, DANI<sub>m</sub> was less sensitive to variation in moisture content due to band placement closer to the center of the SWIR2 spectral region, and produced lower error than CINDI<sub>m</sub>. The water ratio index for CINDI<sub>m</sub> used the 2211 nm reference band

reflectance divided by the 2038 nm reference band reflectance. The water ratio index for DANI<sub>m</sub> used the 2220 nm feature band reflectance divided by the 2145 nm reference band reflectance; other ratios were tested but the ratio of these bands produced the largest reduction in RMSE. When water ratio indices were added to both linear regressions RMSE declined, particularly for wider ranges in RWC (Fig. 9). Due to CINDI<sub>m</sub> bands' higher sensitivity to water content, its water ratio index provided a better correction to the CIBR index relationship with fractional NPV cover. Multiple linear regression using CINDI<sub>m</sub> and its water ratio index produced RMSE ranging from 0.061 for the driest spectra (R<sup>2</sup> = 0.950) to a maximum of 0.075 for 0–90% RWC (R<sup>2</sup> = 0.924).

### 3.6. Continuity analysis

Simulated reflectances for CINDI<sub>m</sub> and DANI<sub>m</sub> bands, calculated from EMIT imagery, were strongly correlated with simulated reflectance from the Landsat 8 OLI SWIR2 band (Table 6). R<sup>2</sup> values exceeded 0.98 for all potential index bands, with the first CINDI<sub>m</sub> reference band (2038 nm) producing the highest RMSE at 0.68% reflectance. The first DANI<sub>m</sub> reference band (2145 nm) was most strongly correlated with Landsat 8 OLI, with a 0.998 R<sup>2</sup> and RMSE at 0.18% reflectance. When all CINDI<sub>m</sub> or DANI<sub>m</sub> bands were included in a multiple linear regression against

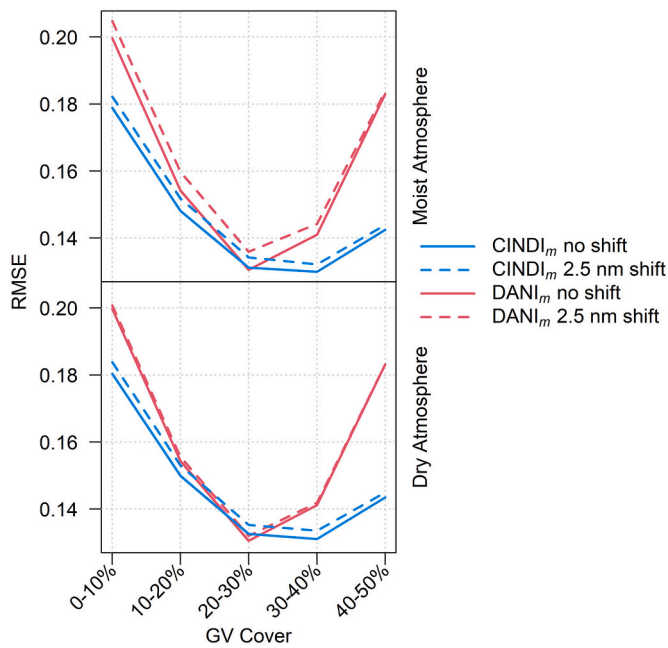


Fig. 8. Error in modeled fractional NPV cover based on reflectance uncertainty and SNR both with and without a modeled 2.5 nm band shift, for different GV cover ranges.

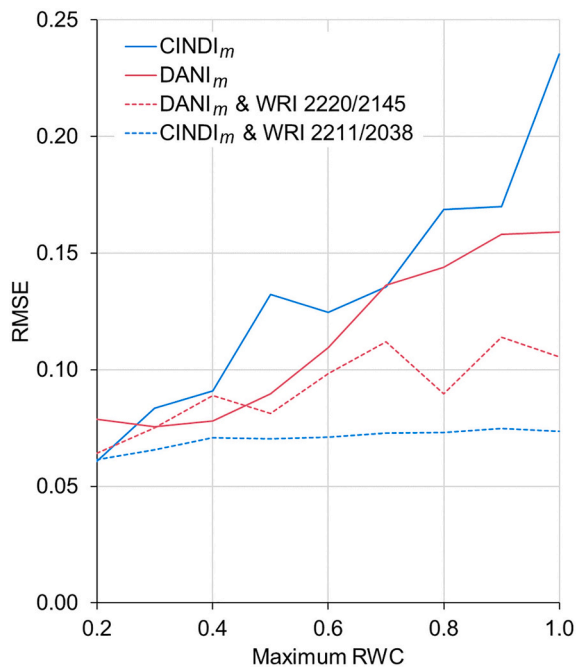


Fig. 9. Fractional NPV cover RMSE for field spectra with varying soil and NPV fraction and RWC from Quemada and Daughtry (2016). WRI is water ratio index. RWC ranges start at 0 and continue through the maximum RWC shown on the x-axis.

simulated Landsat 8 OLI SWIR2, RMSE dropped to <0.1% reflectance.

Despite relatively low RMSE across all CINDI<sub>m</sub> and DANI<sub>m</sub> bands, reflectance error can be much higher for some spectra due to a narrower band’s inability to approximate Landsat 8 OLI’s broadband reflectance. Fig. 10 displays residuals for linear regression models between the two longer wavelength CINDI<sub>m</sub> bands (Fig. 10b, c) and simulated Landsat OLI SWIR2 band reflectance, and between DANI<sub>m</sub> bands (Fig. 10d, e, f) and simulated Landsat OLI SWIR2 band reflectance. For the 2108 band,

Table 6

R<sup>2</sup> and RMSE for EMIT image spectra convolved to Landsat 8 OLI SWIR2 band reflectance, as modeled by CINDI<sub>m</sub> and DANI<sub>m</sub> bands. Similar continuity results for Sentinel-2a MSI SWIR2 band reflectance are shown in Table S1.

Index	Band center wavelength (nm)	R <sup>2</sup>	RMSE
CINDI <sub>m</sub>	2038	0.980	0.0068
CINDI <sub>m</sub>	2108	0.991	0.0042
CINDI <sub>m</sub>	2211	0.992	0.0041
DANI <sub>m</sub>	2145	0.998	0.0018
DANI <sub>m</sub>	2220	0.993	0.0040
DANI <sub>m</sub>	2265	0.995	0.0028
CINDI <sub>m</sub>	all bands	1.000	0.0007
DANI <sub>m</sub>	all bands	1.000	0.0002

areas with high NPV and GV cover had negative residuals, while urban surfaces (which commonly display 2300 nm absorption by carbonate minerals and hydrocarbons due to pervasive use of concrete and plastic) and soils with a 2200 nm absorption feature had positive residuals (Fig. 10b). These trends reversed for the 2211 nm CINDI<sub>m</sub> and 2220 nm DANI<sub>m</sub> bands, with high NPV and GV cover producing positive residuals, and urban and soil surfaces producing negative residuals (Fig. 10c, e). 2145 nm displayed the lowest residuals of any individual band, with the only strong residuals appearing for soil surfaces with mineral absorption near 2200 nm and a photovoltaic solar farm with reduced reflectance at wavelengths beyond 2230 nm. When three index bands were used in multiple linear regressions, residuals dropped to very low levels. All three CINDI<sub>m</sub> bands combined produced the largest residuals for urban surfaces and the solar farm, but residuals were much closer to zero than for any individual band (Fig. 10g). Residuals from all three DANI<sub>m</sub> bands combined were very close to zero, with a weak positive residual from the solar farm producing the only feature of note within the residual image (Fig. 10h).

### 3.7. Estimated NPV cover image qualitative comparison

CINDI<sub>m</sub> proved better at capturing spatial variation in fractional NPV cover within the EMIT scene than DANI<sub>m</sub>. CINDI<sub>m</sub> produced high estimated NPV cover in fallowed fields and areas with senesced grass cover, and low estimated NPV cover in areas with high GV, soil, or impervious surface cover (Fig. 11b). NPV cover estimated using DANI<sub>m</sub> was mostly above 50%, with low NPV cover relegated to areas with exposed soil. DANI<sub>m</sub> strongly overestimated NPV cover in areas with high GV cover (Fig. 11c), consistent with past findings of poor discrimination between NPV and GV cover for indices using the 2300 nm lignocellulose absorption feature (e.g., Lamb et al., 2022; Serbin et al., 2013).

## 4. Discussion

Comparison of error metrics for indices used to estimate NPV cover demonstrated several important findings. First, RMSE values for hyperspectral and multispectral indices were very similar, demonstrating that 10 nm hyperspectral bandpass is not necessary to improve accuracy of index-estimated NPV cover. Second, error was lower for indices utilizing only the 2100 nm lignocellulose absorption feature (e.g., CINDI), with higher RMSE for indices using the 2300 nm feature or both features (e.g., DANI). This difference is consistent with prior investigations (Hively et al., 2021; Lamb et al., 2022), and our results point toward CINDI as being a more robust NPV index when global variability in soils is considered. Third, three-band indices utilizing only the 2100 nm lignocellulose absorption reduced error relative to two-band indices. In contrast, local minimum RMSE was similar for two- and three-band indices applied to the 2300 nm lignocellulose absorption feature or both features. However, a third band (e.g., DANI<sub>m</sub> x band at 2145 nm) did provide an apparent advantage for continuity with heritage Landsat systems. Fourth, ratio-based indices (NDI, RI, and CIBR) were routinely superior for estimating NPV cover compared to

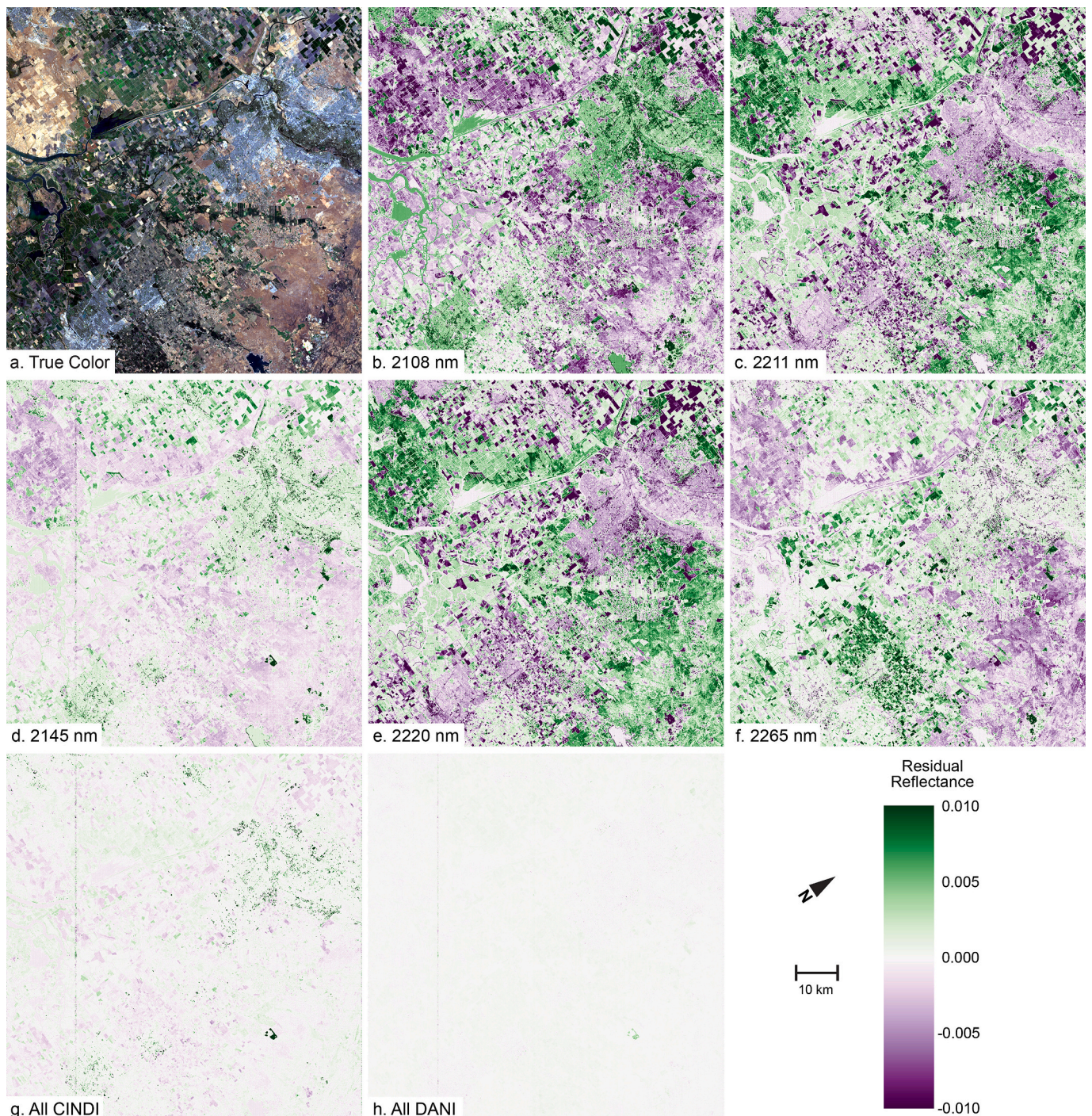


**Fig. 10.** Residuals of EMIT image spectra convolved to Landsat 8 OLI SWIR2 band reflectance, as modeled by b) CINDI<sub>m</sub> feature band y at 2108 nm; c) CINDI<sub>m</sub> reference band z at 2211 nm; d) DANI<sub>m</sub> reference band x at 2145 nm; e) DANI<sub>m</sub> feature band y at 2220 nm; f) DANI<sub>m</sub> reference band z at 2265 nm; g) all CINDI<sub>m</sub> bands; h) all DANI<sub>m</sub> bands. CINDI<sub>m</sub> reference band x (2038 nm) was omitted from the single band comparison images because of its higher residuals compared to other bands. A true color composite of the EMIT tile is shown for reference in (a). All residuals are scaled from -1% to +1% reflectance. The vertical stripe seen in d and g is due to a post-launch change in the EMIT instrument that was uncharacterized by pre-launch calibrations; reduction of this artifact is planned for future data versions (R. Green, personal communication). (For interpretation of the references to color in this figure legend, the reader is referred to the web version of this article.)

difference indices. Lastly, CIBR indices provided the lowest RMSE out of all indices tested. We attribute their improved performance to the use of weighting factors, which can better account for the shape of asymmetrical spectral features.

Based on our results, CINDI is in most ways superior to DANI for estimating fractional NPV cover. Hyperspectral and multispectral versions of CINDI produced the lowest RMSE for modeling the NPV cover of

over a million synthetic mixtures that included a diversity in NPV and soil mineral spectral absorptions. Although CINDI<sub>m</sub> bands were more sensitive to uncertainty in atmospheric conditions, lower error for CINDI<sub>m</sub> persisted when reflectance retrieval uncertainty was included. If CINDI<sub>m</sub> bands are adopted for future multispectral/superspectral satellite missions, band center wavelength and bandwidth for the 2038 nm band will need to be constrained to smaller tolerances than for other

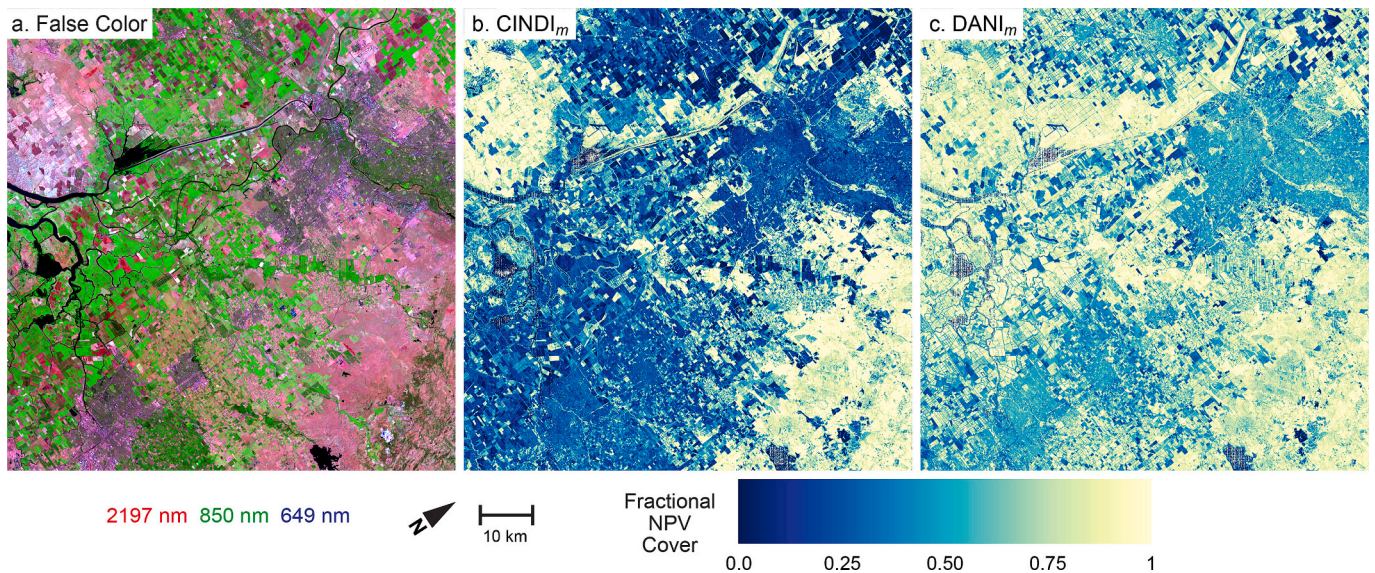


**Fig. 11.** a) A SWIR2/near infrared/false color composite of EMIT scene EMIT\_L2A\_RFL\_001\_20220813T232355\_2222515\_004, and fraction NPV cover estimates using b) CINDI<sub>m</sub> and c) DANI<sub>m</sub>.

bands; this is due to the relatively narrow width of this atmospheric window, higher sensitivity to water vapor, and greater reflectance retrieval uncertainty. Atmospheric correction and reflectance retrieval uncertainty will be important for this band due to variability in atmospheric transmittance at this wavelength. Even when accounting for increased reflectance uncertainty, CINDI<sub>m</sub> had lower RMSE across nearly all soil spectral types, and similar or lower RMSE across a wide range of fractional GV and soil cover. Creating soil spectral class-specific models resulted in small reductions in RMSE for CINDI<sub>m</sub>, while class-specific models may be more necessary to reduce error using DANI. Qualitatively, CINDI<sub>m</sub> was not prone to overestimation of NPV cover in areas with high GV cover. DANI<sub>m</sub> was less sensitive to variability in RWC, but this wasn't a clear advantage of this index. Since CINDI bands are more sensitive to moisture, better correction for RWC was possible using a water ratio index, which by extension could provide additional information about the water status of NPV, soil, and vegetation.

Based on our mixtures of diverse NPV and soil endmembers, a single global relationship using three CINDI<sub>m</sub> bands would be anticipated to have fractional NPV cover error in the range of  $\pm 13$ – $16\%$ . Soil spectral class-specific models would only minimally reduce this uncertainty, with the possible exception of rare mineral absorption features like topaz in soil Class 8. Error may exceed this range for areas of very low GV cover.

Multiple factors could cause NPV cover error to be underestimated by this study. While the soil spectral library captures a diversity of mineral absorption features, it was reliant on previously measured soil spectra and may not represent the actual global frequency distributions of soil mineral absorptions. In particular, tropical soils are likely underrepresented in the source soil spectral libraries. While the SWIR2 spectrum of pure GV is dominated by liquid water absorption, relatively few vegetation types were included in the GV spectral library. Darkening of synthetic mixtures relied on a limited set of land cover types and temporal range. Lower reflectance mixtures may increase RMSE. Linear spectral mixing was assumed, and non-linear mixing may impact error in NPV cover estimation, particularly for high GV fractional cover. More extensive field datasets are needed to enable better quantification of error in NPV cover estimation, and future work should examine the impacts of GV cover exceeding 50%.

Other limitations of this study may have led to overestimation of error in modeled NPV cover. Reflectance uncertainty and SNR were based on a  $60^\circ$  solar zenith angle and 12% surface reflectance. For many

applications, solar zenith angle will frequently be smaller and/or average surface reflectance will be higher, leading to higher SNR and reduced RMSE (Fig. S4). While  $\pm 13$ – $16\%$  error represents large bounds for a potential global model, RMSE for the [Quemada and Daughtry \(2016\)](#) dataset (Section 3.5) demonstrates that site-specific models have the potential to greatly reduce error in estimated NPV cover. For dry soils, CINDI<sub>m</sub> RMSE was approximately 6%, and increased to 7% across the entire range of RWC when CINDI<sub>m</sub> was used with a water ratio index. At the global scale, relative abundances of NPV, soil, and GV fractions may differ from the Dirichlet distribution used in this analysis, which could decrease or increase error in estimated NPV cover. Presence of additional materials not accounted for in NPV-soil-GV mixtures, such as standing water or snow, will likewise have unknown impacts on error in estimated NPV cover.

Our study examined only SWIR2 bands using relatively simple index methods. There is potential for reducing NPV cover error using additional visible, near infrared, and SWIR1 ( $\sim 1400$ – $1800$  nm) bands, or by using complete spectra with more advanced methods like SMA, spectral feature analysis, partial least squares regression, and machine learning ([Dennison et al., 2019](#)). Various forms of SMA have been commonly used for quantifying NPV cover ([Coates et al., 2015](#); [Davidson et al., 2008](#); [Guerschman et al., 2015](#); [Mayes et al., 2015](#); [Numata et al., 2007](#); [Okin, 2007](#); [Pancorbo et al., 2023](#); [Tane et al., 2018](#)). Future applications of SMA may benefit from additional bands capturing the 2100 and 2300 nm lignocellulose absorption features. Linear regression produced estimated NPV cover outside the range of physically possible values (Fig. 6), but methods like SMA or beta regression ([Ferrari and Cribari-Neto, 2004](#)) could be used to constrain estimated NPV cover to between zero and one.

The longer wavelength CINDI<sub>m</sub> reference band at 2211 nm would be sensitive to minerals absorbing in the 2200 nm wavelength region, which include clays, such as montmorillonite and kaolinite, and white micas, such as muscovite and illite. Because the feature band of CINDI<sub>m</sub> at 2108 nm is on the shoulder of the clay/white mica absorption feature, CINDI<sub>m</sub> bands would offer an opportunity to generate a normalized index for absorption by these minerals. Thus CINDI<sub>m</sub> bands could still allow for mineral mapping applications developed using broader SWIR2 band sensitivity to 2200 nm absorption features ([Adiri et al., 2020](#); [Crósta and Filho, 2009](#)). CINDI<sub>m</sub> bands would be relatively insensitive to longer wavelength mineral absorptions (e.g., carbonates and chlorites) and to methane plume emissions ([Jacob et al., 2022](#)).

CINDI<sub>m</sub> bands did provide worse continuity with Landsat OLI when compared to DANI<sub>m</sub> bands. DANI<sub>m</sub>'s 2145 nm reference band had the best single-band correlation with simulated Landsat 8 OLI SWIR2 reflectance. This finding is somewhat counterintuitive since the second CINDI<sub>m</sub> reference band (2211 nm) and DANI<sub>m</sub> feature band (2220 nm) are closer to the nominal center of the Landsat 8 OLI SWIR2 band (2200 nm). However, the 2145 nm band is still well within the OLI SWIR2 band's > 180 nm bandwidth, and the 2145 nm band avoids mineral absorption features at longer wavelengths that reduce correlations between new bands and the heritage band. OLI SWIR2 reflectance cannot be replicated by any single narrower band due to spectral variability in the SWIR2 region, although combinations of three bands can reduce residuals to a very low level. More investigation is needed to determine how changing band centers and bandwidth could impact temporal monitoring applications of Landsat data (e.g., [Eidenshink et al., 2007](#); [Hansen et al., 2017](#); [Kennedy et al., 2014](#)) and "harmonized" multi-sensor products ([Claverie et al., 2018](#)). While continuity issues are important for temporal monitoring applications, new bands will introduce greatly enhanced capabilities for monitoring changes in NPV cover over time, enabling novel land cover, disturbance, agriculture, and wildfire danger applications.

## 5. Conclusions

CINDI, a three-band weighted index sensitive to the 2100 nm lignocellulose absorption feature, provided the best performance for estimating fractional NPV cover when considering a wide range of spectral mixtures that included variability in soil and NPV spectral absorptions. The multispectral version of CINDI was less sensitive to soil spectral absorptions and fractional GV cover than competing indices. While CINDI<sub>m</sub> was more sensitive to soil and NPV RWC, this sensitivity allows for inclusion of a water ratio index capable of correcting errors in estimated NPV cover. Individual CINDI<sub>m</sub> band reflectance did not have the best continuity with the simulated Landsat 8 OLI SWIR2 band reflectance, but multiple bands may be used to adequately approximate heritage reflectance.

Based on our findings, future multispectral or superspectral systems can adopt the three SWIR2 bands used to calculate CINDI<sub>m</sub> to improve global NPV mapping capabilities. Landsat Next is envisioned to include three satellites with 10–20 m spatial resolution visible, near infrared, and SWIR bands, with first launch anticipated by late 2030. Based on the analysis documented in this paper, Landsat Next has adopted the following SWIR2 band specifications in its instrument requirements ([NASA, 2023](#)): a band centered at 2038 nm with 25 nm bandwidth; a band centered at 2108 nm with 40 nm bandwidth; and a band centered at 2211 nm with 40 nm bandwidth. Tolerances for these band center wavelengths are  $\pm 2$  nm for the 2038 nm band and  $\pm 4$  nm for the 2108 and 2211 nm bands, with the tighter tolerance for the 2038 nm band based on atmospheric transmittance. These bands and the associated CINDI index may enable use of Landsat Next data for applications utilizing NPV cover mapping, such as improving soil management, preventing land degradation, evaluating impacts of drought, mapping ecosystem disturbance, and assessing wildfire danger.

Since CINDI can function as a hyperspectral or multispectral index with little change in accuracy of NPV cover estimation, application of CINDI across data from future superspectral sensors and imaging spectrometers will be feasible. Multiple imaging spectroscopy missions are currently on-orbit or planned for launch later this decade ([Green and Thompson, 2020](#); [Guanter et al., 2015](#); [Iwasaki et al., 2011](#); [Loizzo et al., 2018](#); [Rast et al., 2021](#); [Stavros et al., 2023](#)). Their capabilities can be combined with planned next generation superspectral systems like Landsat Next to provide high-frequency monitoring of dynamic NPV cover.

## CRedit authorship contribution statement

**Philip E. Dennison:** Conceptualization, Methodology, Software, Validation, Formal analysis, Writing – original draft, Writing – review & editing, Visualization, Project administration. **Brian T. Lamb:** Methodology, Software, Formal analysis, Writing – original draft, Writing – review & editing. **Michael J. Campbell:** Methodology, Software, Formal analysis, Writing – review & editing, Visualization. **Raymond F. Kokaly:** Methodology, Software, Formal analysis, Writing – review & editing. **W. Dean Hively:** Writing – review & editing. **Eric Vermote:** Software, Formal analysis, Writing – review & editing. **Phil Dabney:** Formal analysis, Writing – review & editing. **Guy Serbin:** Writing – review & editing. **Miguel Quemada:** Validation, Writing – review & editing. **Craig S.T. Daughtry:** Writing – review & editing. **Jeffrey Masek:** Writing – review & editing. **Zhuoting Wu:** Writing – review & editing.

## Declaration of Competing Interest

The authors declare that they have no known competing financial interests or personal relationships that could have appeared to influence the work reported in this paper.

## Data availability

USGS Data Release planned following publication.

## Acknowledgements

We are grateful to Petya Campbell, Michael Marshall, Dar Roberts, and Keely Roth for sharing their field spectra and data. Use of trade, product, or firm names is for information purposes only and does not constitute an endorsement by the U.S. Government. Brian Lamb and Dean Hively are supported by the USGS National Land Imaging and Land Change Science programs. Raymond Kokaly is supported by funding from the USGS National Land Imaging Program through the Earth Resources Observation and Science Center Hyperspectral Imaging project.

## Appendix A. Supplementary data

Supplementary data to this article can be found online at <https://doi.org/10.1016/j.rse.2023.113715>.

## References

- Adiri, Z., Lhissou, R., El Harti, A., Jellouli, A., Chakouri, M., 2020. Recent advances in the use of public domain satellite imagery for mineral exploration: A review of Landsat-8 and Sentinel-2 applications. *Ore Geol. Rev.* 117, 103332 <https://doi.org/10.1016/j.oregeorev.2020.103332>.
- Asner, G.P., Lobell, D.B., 2000. A biogeophysical approach for automated SWIR unmixing of soils and vegetation. *Remote Sens. Environ.* 74, 99–112. [https://doi.org/10.1016/S0034-4257\(00\)00126-7](https://doi.org/10.1016/S0034-4257(00)00126-7).
- Azzari, G., Grassini, P., Edreira, J.I.R., Conley, S., Mourtzinis, S., Lobell, D.B., 2019. Satellite mapping of tillage practices in the North Central US region from 2005 to 2016. *Remote Sens. Environ.* 221, 417–429. <https://doi.org/10.1016/j.rse.2018.11.010>.
- Bai, X., Zhao, W., Ji, S., Qiao, R., Dong, C., Chang, X., 2021. Estimating fractional cover of non-photosynthetic vegetation for various grasslands based on CAI and DFI. *Ecol. Indic.* 131, 108252 <https://doi.org/10.1016/j.ecolind.2021.108252>.
- Bannari, A., Pacheco, A., Staenz, K., McNairn, H., Omari, K., 2006. Estimating and mapping crop residues cover on agricultural lands using hyperspectral and IKONOS data. *Remote Sens. Environ.* 104, 447–459. <https://doi.org/10.1016/j.rse.2006.05.018>.
- Beeson, P.C., Daughtry, C.S.T., Wallander, S.A., 2020. Estimates of conservation tillage practices using Landsat archive. *Remote Sens.* 12, 2665. <https://doi.org/10.3390/rs12162665>.
- Berk, A., Conforti, P., Kennett, R., Perkins, T., Hawes, F., Van Den Bosch, J., 2014. MODTRAN® 6: A major upgrade of the MODTRAN® radiative transfer code. In: *2014 6th Workshop on Hyperspectral Image and Signal Processing: Evolution in Remote Sensing (WHISPERS)*. IEEE, pp. 1–4.

- Blanco-Canqui, H., Wortmann, C.S., 2020. Does occasional tillage undo the ecosystem services gained with no-till? A review. *Soil Tillage Res.* 198, 104534 <https://doi.org/10.1016/j.still.2019.104534>.
- Borel, C.C., Gerstl, S.A.W., 1994. Nonlinear spectral mixing models for vegetative and soil surfaces. *Remote Sens. Environ.* 47, 403–416. [https://doi.org/10.1016/0034-4257\(94\)90107-4](https://doi.org/10.1016/0034-4257(94)90107-4).
- Brown, D.J., Shepherd, K.D., Walsh, M.G., Dewayne Mays, M., Reinsch, T.G., 2006. Global soil characterization with VNIR diffuse reflectance spectroscopy. *Geoderma* 132, 273–290. <https://doi.org/10.1016/j.geoderma.2005.04.025>.
- Chambers, J.Q., Fisher, J.L., Zeng, H., Chapman, E.L., Baker, D.B., Hurrut, G.C., 2007. Hurricane Katrina's carbon footprint on U.S. Gulf Coast forests. *Science* 318, 1107. <https://doi.org/10.1126/science.1148913>.
- Clark, R.N., 1999. Spectroscopy of rocks and minerals, and principles of spectroscopy. In: *Manual of Remote Sensing*. John Wiley and Sons, New York, pp. 3–58.
- Claverie, M., Ju, J., Masek, J.G., Dungan, J.L., Vermote, E.F., Roger, J.-C., Skakun, S.V., Justice, C., 2018. The harmonized Landsat and Sentinel-2 surface reflectance data set. *Remote Sens. Environ.* 219, 145–161. <https://doi.org/10.1016/j.rse.2018.09.002>.
- Coates, A.R., Dennison, P.E., Roberts, D.A., Roth, K.L., 2015. Monitoring the impacts of severe drought on southern California chaparral species using hyperspectral and thermal infrared imagery. *Remote Sens.* 7, 14276–14291. <https://doi.org/10.3390/rs71114276>.
- Crósta, A.P., Filho, C.R.D.S., 2009. Mineral exploration with landsat thematic mapper (TM)/enhanced thematic mapper plus (ETM+): a review of the fundamentals, characteristics, data processing, and case studies. In: Bedell, R., Crósta, A.P., Grunsky, E. (Eds.), *Remote Sensing and Spectral Geology*. Society of Economic Geologists, p. 0. <https://doi.org/10.5382/Rev.16.06>.
- Daughtry, C.S.T., 2001. Discriminating crop residues from soil by shortwave infrared reflectance. *Agron. J.* 93, 125–131. <https://doi.org/10.2134/agronj2001.931125x>.
- Daughtry, C.S.T., Hunt, E.R., 2008. Mitigating the effects of soil and residue water contents on remotely sensed estimates of crop residue cover. *Remote Sens. Environ. Remote Sens. Data Assimilat. Spec. Issue* 112, 1647–1657. <https://doi.org/10.1016/j.rse.2007.08.006>.
- Daughtry, C.S.T., Hunt, E.R., Doraiswamy, P.C., McMurtrey, J.E., 2005. Remote sensing the spatial distribution of crop residues. *Agron. J.* 97, 864–871. <https://doi.org/10.2134/agronj2003.0291>.
- Daughtry, C.S.T., Doraiswamy, P.C., Hunt, E.R., Stern, A.J., McMurtrey, J.E., Prueger, J. H., 2006. Remote sensing of crop residue cover and soil tillage intensity. *Soil Tillage Res.* 91, 101–108. <https://doi.org/10.1016/j.still.2005.11.013>.
- Davidson, E.A., Asner, G.P., Stone, T.A., Neill, C., Figueiredo, R.O., 2008. Objective indicators of pasture degradation from spectral mixture analysis of Landsat imagery. *J. Geophys. Res. Biogeosci.* 113 <https://doi.org/10.1029/2007.JG000622>.
- Demattê, J.A.M., Dotto, A.C., Paiva, A.F.S., Sato, M.V., Dalmolin, R.S.D., de Araújo, M., da Silva, E.B., Nanni, M.R., ten Caten, A., Noronha, N.C., Lacerda, M.P.C., de Araújo Filho, J.C., Rizzo, R., Bellinaso, H., Francolino, M.R., Schaefer, C.E.G.R., Vicente, L. E., dos Santos, U.J., de Sá Barretto Sampaio, E.V., Menezes, R.S.C., de Souza, J.J.L.L., Abrahão, W.A.P., Coelho, R.M., Grego, C.R., Lani, J.L., Fernandes, A.R., Gonçalves, D.A.M., Silva, S.B.G., de Menezes, M.D., Curi, N., Couto, E.G., dos Anjos, L.H.C., Ceddia, M.H., Pinheiro, É.F.M., Grunwald, S., Vasques, G.M., Marques Júnior, J., da Silva, A.J., Barreto, M.C.V., Nóbrega, G.N., da Silva, M.Z., de Souza, S. F., Valladares, G.S., Viana, J.H.M., da Silva Terra, F., Horák-Terra, I., Fiorio, P.R., da Silva, R.C., Frade Júnior, E.F., Lima, R.H.C., Alba, J.M.F., de Souza Junior, V.S., Brefin, M.D.L.M.S., Ruivo, M.D.L.P., Ferreira, T.O., Brait, M.A., Caetano, N.R., Bringhenti, I., de Sousa Mendes, W., Saffanelli, J.L., Guimarães, C.C.B., Poppeli, R.R., Souza, A.B., Quesada, C.A., do Couto, H.T.Z., 2019. The Brazilian Soil Spectral Library (BSSL): A general view, application and challenges. *Geoderma* 354, 113793. <https://doi.org/10.1016/j.geoderma.2019.05.043>.
- Dennison, P.E., 2006. Fire detection in imaging spectrometer data using atmospheric carbon dioxide absorption. *Int. J. Remote Sens.* 27, 3049–3055. <https://doi.org/10.1080/014311606006060871>.
- Dennison, P.E., Qi, Y., Meerdink, S.K., Kokaly, R.F., Thompson, D.R., Daughtry, C.S.T., Quemada, M., Roberts, D.A., Gader, P.D., Wetherley, E.B., Numata, I., Roth, K.L., 2019. Comparison of methods for modeling fractional cover using simulated satellite hyperspectral imager spectra. *Remote Sens.* 11, 2072. <https://doi.org/10.3390/rs11182072>.
- Eidenshink, J., Schwind, B., Brewer, K., Zhu, Z.-L., Quayle, B., Howard, S., 2007. A project for monitoring trends in burn severity. *Fire Ecol.* 3, 3–21. <https://doi.org/10.4996/fireecology.0301003>.
- Elmore, A.J., Asner, G.P., Hughes, R.F., 2005. Satellite monitoring of vegetation phenology and fire fuel conditions in Hawaiian drylands. *Earth Interact.* 9, 1–21. <https://doi.org/10.1175/EI160.1>.
- Elvidge, C.D., 1990. Visible and near infrared reflectance characteristics of dry plant materials. *Int. J. Remote Sens.* 11, 1775–1795. <https://doi.org/10.1080/01431169008955129>.
- Ferrari, S., Cribari-Neto, F., 2004. Beta regression for modelling rates and proportions. *J. Appl. Stat.* 31, 799–815. <https://doi.org/10.1080/0266476042000214501>.
- GeoCradle, 2021. Regional Soil Spectral Library [WWW Document]. URL <http://datahub.geocradle.eu/dataset/regional-soil-spectral-library>.
- Goward, S.N., Masek, J.G., Williams, D.L., Irons, J.R., Thompson, R.J., 2001. The Landsat 7 mission: Terrestrial research and applications for the 21st century. *Remote Sens. Environ. Landsat 7* (78), 3–12. [https://doi.org/10.1016/S0034-4257\(01\)00262-0](https://doi.org/10.1016/S0034-4257(01)00262-0).
- Graham, G.E., Kokaly, R.F., Kelley, K.D., Hoefen, T.M., Johnson, M.R., Hubbard, B.E., 2018. Application of imaging spectroscopy for mineral exploration in Alaska: A study over porphyry Cu deposits in the Eastern Alaska Range. *Econ. Geol.* 113, 489–510. <https://doi.org/10.5382/ecogeo.2018.4559>.
- Green, R.O., Thompson, D.R., 2020. An Earth science imaging spectroscopy mission: The Earth Surface Mineral Dust Source Investigation (EMIT). In: *IGARSS 2020 - 2020 IEEE International Geoscience and Remote Sensing Symposium*. Presented at the IGARSS 2020 - 2020 IEEE International Geoscience and Remote Sensing Symposium, pp. 6262–6265. <https://doi.org/10.1109/IGARSS39084.2020.9323741>.
- Green, R.O., Carrere, V., Conel, J.E., 1989. Measurement of atmospheric water vapor using the Airborne Visible/Infrared Imaging Spectrometer. In: *Proceedings of the ASPRS Conference on Imaging Processing*. American Society for Photogrammetry and Remote Sensing, Sparks, Nevada, USA.
- Green, R.O., Eastwood, M.L., Sarture, C.M., Chrien, T.G., Aronsson, M., Chippendale, B. J., Faust, J.A., Pavri, B.E., Chovit, C.J., Solis, M., Olah, M.R., Williams, O., 1998. Imaging spectroscopy and the Airborne Visible/Infrared Imaging Spectrometer (AVIRIS). *Remote Sens. Environ.* 65, 227–248. [https://doi.org/10.1016/S0034-4257\(98\)00064-9](https://doi.org/10.1016/S0034-4257(98)00064-9).
- Guanter, L., Kaufmann, H., Segl, K., Foerster, S., Rogass, C., Chabrilat, S., Kuester, T., Hollstein, A., Rossner, G., Chlebek, C., Straif, C., Fischer, S., Schrader, S., Storch, T., Heiden, U., Mueller, A., Bachmann, M., Mühle, H., Müller, R., Habermeyer, M., Ohndorf, A., Hill, J., Buddenbaum, H., Hostert, P., Van der Linden, S., Leitão, P.J., Rabe, A., Doerffer, R., Krasemann, H., Xi, H., Mauser, W., Hank, T., Locher, M., Rast, M., Staenz, K., Sang, B., 2015. The EnMAP spaceborne imaging spectroscopy mission for earth observation. *Remote Sens.* 7, 8830–8857. <https://doi.org/10.3390/rs70708830>.
- Guerschman, J.P., Scarth, P.F., McVicar, T.R., Renzullo, L.J., Malthus, T.J., Stewart, J.B., Rickards, J.E., Trevithick, R., 2015. Assessing the effects of site heterogeneity and soil properties when unmixing photosynthetic vegetation, non-photosynthetic vegetation and bare soil fractions from Landsat and MODIS data. *Remote Sens. Environ.* 161, 12–26. <https://doi.org/10.1016/j.rse.2015.01.021>.
- Hansen, C.H., Burian, S.J., Dennison, P.E., Williams, G.P., 2017. Spatiotemporal variability of lake water quality in the context of remote sensing models. *Remote Sens.* 9 <https://doi.org/10.3390/rs9050409>.
- Hively, W.D., Lamb, B.T., Daughtry, C.S.T., Shermeyer, J., McCarty, G.W., Quemada, M., 2018. Mapping crop residue and tillage intensity using WorldView-3 satellite shortwave infrared residue indices. *Remote Sens.* 10, 1657. <https://doi.org/10.3390/rs10101657>.
- Hively, W.D., Shermeyer, J., Lamb, B.T., Daughtry, C.T., Quemada, M., Keppler, J., 2019. Mapping crop residue by combining Landsat and WorldView-3 satellite imagery. *Remote Sens.* 11, 1857. <https://doi.org/10.3390/rs11161857>.
- Hively, W.D., Lamb, B.T., Daughtry, C.S.T., Serbin, G., Dennison, P., Kokaly, R.F., Wu, Z., Masek, J.G., 2021. Evaluation of SWIR crop residue bands for the Landsat Next mission. *Remote Sens.* 13, 3718. <https://doi.org/10.3390/rs13183718>.
- Hobbie, S.E., 2015. Plant species effects on nutrient cycling: revisiting litter feedbacks. *Trends Ecol. Evol.* 30, 357–363. <https://doi.org/10.1016/j.tree.2015.03.015>.
- Iwasaki, A., Ohgi, N., Tanii, J., Kawashima, T., Inada, H., 2011. Hyperspectral Imager Suite (HISUI)-Japanese hyper-multi spectral radiometer. In: 2011 IEEE International Geoscience and Remote Sensing Symposium. Presented at the 2011 IEEE International Geoscience and Remote Sensing Symposium, pp. 1025–1028. <https://doi.org/10.1109/IGARSS.2011.6049308>.
- Jacob, D.J., Varon, D.J., Cusworth, D.H., Dennison, P.E., Frankenberg, C., Gautam, R., Guanter, L., Kelley, J., McKeever, J., Ott, L.E., Poulter, B., Qu, Z., Thorpe, A.K., Worden, J.R., Duren, R.M., 2022. Quantifying methane emissions from the global scale down to point sources using satellite observations of atmospheric methane. *Atmos. Chem. Phys.* 22, 9617–9646. <https://doi.org/10.5194/acp-22-9617-2022>.
- Lin, X., Ma, J., Wen, Z., Song, K., 2015. Estimation of maize residue cover using Landsat-8 OLI image spectral information and textural features. *Remote Sens.* 7, 14559–14575. <https://doi.org/10.3390/rs71114559>.
- Lin, S., Homer, C., Yang, L., Danielson, P., Dewitz, J., Li, C., Zhu, Z., Xian, G., Howard, D., 2019. Overall methodology design for the United States national land cover database 2016 products. *Remote Sens.* 11, 2971. <https://doi.org/10.3390/rs11242971>.
- Kennedy, R.E., Andréfouët, S., Cohen, W.B., Gómez, C., Griffiths, P., Hais, M., Healey, S. P., Helmer, E.H., Hostert, P., Lyons, M.B., Meigs, G.W., Pflugmacher, D., Phinn, S.R., Powell, S.L., Scarth, P., Sen, S., Schroeder, T.A., Schneider, A., Sonnenschein, R., Vogelmann, J.E., Wulder, M.A., Zhu, Z., 2014. Bringing an ecological view of change to Landsat-based remote sensing. *Front. Ecol. Environ.* 12, 339–346. <https://doi.org/10.1890/1523-1739-2014-0066>.
- Kokaly, R.F., 2011. PRISM: Processing Routines in IDL for Spectroscopic Measurements (Installation Manual and User's Guide, Version 1.0) (No. Open-File Report 2011-1155). U.S. Geological Survey.
- Kokaly, R.F., Clark, R.N., 1999. Spectroscopic determination of leaf biochemistry using band-depth analysis of absorption features and stepwise multiple linear regression. *Remote Sens. Environ.* 67, 267–287. [https://doi.org/10.1016/S0034-4257\(98\)00084-4](https://doi.org/10.1016/S0034-4257(98)00084-4).
- Kokaly, R.F., Skidmore, A.K., 2015. Plant phenolics and absorption features in vegetation reflectance spectra near 1.66  $\mu\text{m}$ . *Int. J. Appl. Earth Obs. Geoinf.* 43, 55–83. <https://doi.org/10.1016/j.jag.2015.01.010>.
- Kokaly, R.F., Asner, G.P., Ollinger, S.V., Martin, M.E., Wessman, C.A., 2009. Characterizing canopy biochemistry from imaging spectroscopy and its application to ecosystem studies. *Remote Sens. Environ. Imaging Spectrosc. Spec. Issue* 113, S78–S91. <https://doi.org/10.1016/j.rse.2008.10.018>.
- Kokaly, R.F., Couvillion, B.R., Holloway, J.M., Roberts, D.A., Ustin, S.L., Peterson, S.H., Khanna, S., Piazza, S.C., 2013. Spectroscopic remote sensing of the distribution and persistence of oil from the Deepwater Horizon spill in Barataria Bay marshes. *Remote Sens. Environ.* 129, 210–230. <https://doi.org/10.1016/j.rse.2012.10.028>.
- Laamrani, A., Joosse, P., McNairn, H., Berg, A.A., Hagerman, J., Powell, K., Berry, M., 2020. Assessing soil cover levels during the non-growing season using multi-temporal satellite imagery and spectral unmixing techniques. *Remote Sens.* 12, 1397. <https://doi.org/10.3390/rs12091397>.

- Lal, R., 1995. The role of residues management in sustainable agricultural systems. *J. Sustain. Agric.* 5, 51–78. [https://doi.org/10.1300/J064v05n04\\_06](https://doi.org/10.1300/J064v05n04_06).
- Lamb, B.T., Dennison, P.E., Hively, W.D., Kokaly, R.F., Serbin, G., Wu, Z., Dabney, P.W., Masek, J.G., Campbell, M., Daughtry, C.S.T., 2022. Optimizing Landsat Next shortwave infrared bands for crop residue characterization. *Remote Sens.* 14, 6128. <https://doi.org/10.3390/rs14236128>.
- Lau, I., Bateman, R., Beattie, E., Caritat, P., Thomas, M., Ong, C., Laukamp, C., Caccetta, M., Wang, R., Cudahy, T., 2019. National Geochemical Survey of Australia Reflectance Spectroscopy Measurements. <https://doi.org/10.25919/5cd8a18939c29>.
- Loizzo, R., Guarini, R., Longo, F., Scopa, T., Formaro, R., Facchinetti, C., Varacalli, G., 2018. Prisma: The Italian hyperspectral mission. In: IGARSS 2018 - 2018 IEEE International Geoscience and Remote Sensing Symposium. Presented at the IGARSS 2018 - 2018 IEEE International Geoscience and Remote Sensing Symposium, pp. 175–178. <https://doi.org/10.1109/IGARSS.2018.8518512>.
- Makarau, A., Richter, R., Schläpfer, D., Reinartz, P., 2017. APDA water vapor retrieval validation for Sentinel-2 imagery. *IEEE Geosci. Remote Sens. Lett.* 14, 227–231. <https://doi.org/10.1109/LGRS.2016.2635942>.
- Marslett, R.C., Qi, J., Heilman, P., Biedenbender, S.H., Carolyn Watson, M., Amer, S., Weltz, M., Goodrich, D., Marslett, R., 2006. Remote sensing for grassland management in the arid Southwest. *Rangel. Ecol. Manag.* 59, 530–540. <https://doi.org/10.2111/05-201R.1>.
- Marshall, M., Thenkabail, P., 2014. Biomass modeling of four leading world crops using hyperspectral narrowbands in support of Hyps IRI Mission. *Photogramm. Eng. Remote Sens.* 80, 757–772.
- Masek, J.G., Wulder, M.A., Markham, B., McCorkel, J., Crawford, C.J., Storey, J., Jenstrom, D.T., 2020. Landsat 9: Empowering open science and applications through continuity. *Remote Sens. Environ.* 248, 111968. <https://doi.org/10.1016/j.rse.2020.111968>.
- Mayes, M.T., Mustard, J.F., Melillo, J.M., 2015. Forest cover change in Miombo Woodlands: modeling land cover of African dry tropical forests with linear spectral mixture analysis. *Remote Sens. Environ.* 165, 203–215. <https://doi.org/10.1016/j.rse.2015.05.006>.
- Meerdink, S., Roberts, D., Hulley, G., Gader, P., Pisek, J., Adamson, K., King, J., Hook, S. J., 2019. Plant species' spectral emissivity and temperature using the hyperspectral thermal emission spectrometer (HyTES) sensor. *Remote Sens. Environ.* 224, 421–435. <https://doi.org/10.1016/j.rse.2019.02.009>.
- Mika, A.M., 1997. Three decades of Landsat instruments. *Photogramm. Eng. Remote Sens.* 63, 839–852.
- Moskowitz, B.M., Reynolds, R.L., Goldstein, H.L., Berquó, T.S., Kokaly, R.F., Bristow, C. S., 2016. Iron oxide minerals in dust-source sediments from the Bodélé Depression, Chad: Implications for radiative properties and Fe bioavailability of dust plumes from the Sahara. *Aeolian Res.* 22, 93–106. <https://doi.org/10.1016/j.aeolia.2016.07.001>.
- Nagler, P.L., Daughtry, C.S.T., Goward, S.N., 2000. Plant litter and soil reflectance. *Remote Sens. Environ.* 71, 207–215. [https://doi.org/10.1016/S0034-4257\(99\)00082-6](https://doi.org/10.1016/S0034-4257(99)00082-6).
- Nagler, P.L., Inoue, Y., Glenn, E.P., Russ, A.L., Daughtry, C.S.T., 2003. Cellulose absorption index (CAI) to quantify mixed soil-plant litter scenes. *Remote Sens. Environ.* 87, 310–325. <https://doi.org/10.1016/j.rse.2003.06.001>.
- Najafi, P., Navid, H., Feizizadeh, B., Eskandari, I., Blaschke, T., 2019. Fuzzy object-based image analysis methods using Sentinel-2A and Landsat-8 data to map and characterize soil surface residue. *Remote Sens.* 11, 2583. <https://doi.org/10.3390/rs11122583>.
- NASA (National Aeronautics and Space Administration), 2023. Landsat Next Instrument Suite (LandIS) Request for Proposal. <https://sam.gov/opp/a90dd64dcf5048678aca1ad1cc22c9e4/view> visited 6/18/2023.
- NEON, 2022. National Ecological Observatory Network Spectrometer orthorectified surface directional reflectance - flightline (DP1.30006.001). [WWW Document]. URL: <https://data.neonscience.org> (accessed 2.9.22).
- Numata, I., Roberts, D.A., Chadwick, O.A., Schimel, J., Sampaio, F.R., Leonidas, F.C., Soares, J.V., 2007. Characterization of pasture biophysical properties and the impact of grazing intensity using remotely sensed data. *Remote Sens. Environ.* 109, 314–327. <https://doi.org/10.1016/j.rse.2007.01.013>.
- Okin, G.S., 2007. Relative spectral mixture analysis — A multitemporal index of total vegetation cover. *Remote Sens. Environ.* 106, 467–479. <https://doi.org/10.1016/j.rse.2006.09.018>.
- Okin, G.S., 2010. The contribution of brown vegetation to vegetation dynamics. *Ecology* 91, 743–755. <https://doi.org/10.1890/09-0302.1>.
- Orgiazzi, A., Ballabio, C., Panagos, P., Jones, A., Fernández-Ugalde, O., 2018. LUCAS Soil, the largest expandable soil dataset for Europe: a review. *Eur. J. Soil Sci.* 69, 140–153. <https://doi.org/10.1111/ejss.12499>.
- Pancorbo, J.L., Quemada, M., Roberts, D.A., 2023. Drought impact on cropland use monitored with AVIRIS imagery in Central Valley, California. *Sci. Total Environ.* 859, 160198. <https://doi.org/10.1016/j.scitotenv.2022.160198>.
- Quemada, M., Daughtry, C.S.T., 2016. Spectral indices to improve crop residue cover estimation under varying moisture conditions. *Remote Sens.* 8, 660. <https://doi.org/10.3390/rs8080660>.
- Quemada, M., Hively, W.D., Daughtry, C.S.T., Lamb, B.T., Shermeyer, J., 2018. Improved crop residue cover estimates obtained by coupling spectral indices for residue and moisture. *Remote Sens. Environ.* 206, 33–44. <https://doi.org/10.1016/j.rse.2017.12.012>.
- Quintano, C., Fernández-Manso, A., Roberts, D.A., 2013. Multiple Endmember Spectral Mixture Analysis (MESMA) to map burn severity levels from Landsat images in Mediterranean countries. *Remote Sens. Environ.* 136, 76–88. <https://doi.org/10.1016/j.rse.2013.04.017>.
- Rast, M., Nieke, J., Adams, J., Isola, C., Gascon, F., 2021. Copernicus Hyperspectral Imaging Mission for the Environment (Chime). In: 2021 IEEE International Geoscience and Remote Sensing Symposium IGARSS. Presented at the 2021 IEEE International Geoscience and Remote Sensing Symposium IGARSS, pp. 108–111. <https://doi.org/10.1109/IGARSS47720.2021.9553319>.
- Ren, H., Zhou, G., Zhang, F., Zhang, X., 2012. Evaluating cellulose absorption index (CAI) for non-photosynthetic biomass estimation in the desert steppe of Inner Mongolia. *Chin. Sci. Bull.* 57, 1716–1722. <https://doi.org/10.1007/s11434-012-5016-3>.
- Reynolds, R.L., Goldstein, H.L., Moskowitz, B.M., Bryant, A.C., Skiles, S.M., Kokaly, R.F., Flagg, C.B., Yauk, K., Berquó, T., Breit, G., Ketterer, M., Fernandez, D., Miller, M.E., Painter, T.H., 2014. Composition of dust deposited to snow cover in the Wasatch Range (Utah, USA): Controls on radiative properties of snow cover and comparison to some dust-source sediments. *Aeolian Res.* 15, 73–90. <https://doi.org/10.1016/j.aeolia.2013.08.001>.
- Reynolds, R.L., Goldstein, H.L., Moskowitz, B.M., Kokaly, R.F., Munson, S.M., Solheid, P., Breit, G.N., Lawrence, C.R., Derry, J., 2020. Dust deposited on snow cover in the San Juan Mountains, Colorado, 2011–2016: Compositional variability bearing on snow-melt effects. *J. Geophys. Res.-Atmos.* 125, e2019JD032210. <https://doi.org/10.1029/2019JD032210>.
- Roberts, D.A., Smith, M.O., Adams, J.B., 1993. Green vegetation, nonphotosynthetic vegetation, and soils in AVIRIS data. *Remote Sens. Environ. Airbone Imaging Spectrom.* 44, 255–269. [https://doi.org/10.1016/0034-4257\(93\)90020-X](https://doi.org/10.1016/0034-4257(93)90020-X).
- Roberts, D.A., Ustin, S.L., Ogunjemiyo, S., Greenberg, J., Dobrowski, S.Z., Chen, J., Hinckley, T.M., 2004. Spectral and structural measures of Northwest forest vegetation at leaf to landscape scales. *Ecosystems* 7, 545–562. <https://doi.org/10.1007/s10021-004-0144-5>.
- Roberts, D.A., Dennison, P.E., Peterson, S., Sweeney, S., Rechel, J., 2006. Evaluation of Airborne Visible/Infrared Imaging Spectrometer (AVIRIS) and Moderate Resolution Imaging Spectrometer (MODIS) measures of live fuel moisture and fuel condition in a shrubland ecosystem in southern California. *J. Geophys. Res. Biogeosci.* 111. <https://doi.org/10.1029/2005JG000113>. G04S02.
- Scarth, P., Denham, R., Watson, F., 2022. JRSRP Fractional Cover 3.0. <https://doi.org/10.5281/zenodo.7008343>.
- Serbin, G., Daughtry, C.S.T., Hunt Jr., E.R., Brown, D.J., McCarty, G.W., 2009a. Effect of soil spectral properties on remote sensing of crop residue cover. *Soil Sci. Soc. Am. J.* 73, 1545–1558. <https://doi.org/10.2136/sssaj2008.0311>.
- Serbin, G., Hunt, E.R., Daughtry, C.S.T., McCarty, G.W., Doraiswamy, P.C., 2009b. An improved ASTER index for remote sensing of crop residue. *Remote Sens.* 1, 971–991. <https://doi.org/10.3390/rs1040971>.
- Serbin, G., Hunt Jr., E.R., Daughtry, C.S.T., McCarty, G.W., 2013. Assessment of spectral indices for crop estimation of senescent vegetation. *Remote Sens. Lett.* 4, 552–560.
- Somers, B., Cools, K., Delalieux, S., Stuckens, J., Van der Zande, D., Verstraeten, W.W., Coppin, P., 2009. Nonlinear Hyperspectral Mixture Analysis for tree cover estimates in orchards. *Remote Sens. Environ.* 113, 1183–1193. <https://doi.org/10.1016/j.rse.2009.02.003>.
- Stavros, E.N., Chrono, J., Cawse-Nicholson, K., Freeman, A., Glenn, N.F., Guild, L., Kokaly, R., Lee, C., Luvall, J., Pavlick, R., Poulter, B., Schollaert Uz, S., Serbin, S., Thompson, D.R., Townsend, P.A., Turpie, K., Yuen, K., Thome, K., Wang, W., Zareh, S.-K., Nastal, J., Bearden, D., Miller, C.E., Schimel, D., 2023. Designing an Observing System to Study the Surface Biology and Geology (SBG) of the Earth in the 2020s. *Journal of Geophysical Research. Biogeosciences* 128, e2021JG006471. <https://doi.org/10.1029/2021JG006471>.
- Tane, Z., Roberts, D., Koltunov, A., Sweeney, S., Ramirez, C., 2018. A framework for detecting conifer mortality across an ecoregion using high spatial resolution spaceborne imaging spectroscopy. *Remote Sens. Environ.* 209, 195–210. <https://doi.org/10.1016/j.rse.2018.02.073>.
- US Geological Survey, 2023. Landsat Next [WWW Document]. URL (accessed 3.1.23). <https://www.usgs.gov/landsat-missions/landsat-next>.
- Van Deventer, A.P., Ward, A.D., Gowda, P.H., Lyon, J.G., 1997. Using Thematic Mapper data to identify contrasting soil plains and tillage practices. *Photogramm. Eng. Remote Sens.* 63, 87–93.
- Vermote, E.F., Tanre, D., Deuze, J.L., Herman, M., Morcette, J.-J., 1997. Second Simulation of the Satellite Signal in the Solar Spectrum, 6S: an overview. *IEEE Trans. Geosci. Remote Sens.* 35, 675–686. <https://doi.org/10.1109/36.581987>.
- Viscarra Rossel, R.A., Behrens, T., Ben-Dor, E., Brown, D.J., Dematté, J.A.M., Shepherd, K.D., Shi, Z., Stenberg, B., Stevens, A., Adamchuk, V., Aichi, H., Barthès, B.G., Bartholomeus, H.M., Bayer, A.D., Bernoux, M., Böttcher, K., Brodský, L., Du, C.W., Chappell, A., Fouad, Y., Genot, V., Gomez, C., Grunwald, S., Gubler, A., Guerrero, C., Hedley, C.B., Knadel, M., Morrás, H.J.M., Nocita, M., Ramirez-Lopez, L., Roudier, P., Campos, E.M.R., Sanborn, P., Sellitto, V.M., Sudduth, K.A., Rawlins, B.G., Walter, C., Winowiecki, L.A., Hong, S.Y., Ji, W., 2016. A global spectral library to characterize the world's soil. *Earth Sci. Rev.* 155, 198–230. <https://doi.org/10.1016/j.earscirev.2016.01.012>.
- World Agroforestry (ICRAF), International Soil Reference and Information Centre (ISRIC), 2021. ICRAF-ISRIC Soil VNIR Spectral Library. <https://doi.org/10.34725/DVN/MFHA9C>.
- Yue, J., Tian, Q., Dong, X., Xu, K., Zhou, C., 2019. Using hyperspectral crop residue angle index to estimate maize and winter-wheat residue cover: A laboratory study. *Remote Sens.* 11, 807. <https://doi.org/10.3390/rs11070807>.
- Zheng, B., Campbell, J.B., Serbin, G., Daughtry, C.S.T., 2013. Multitemporal remote sensing of crop residue cover and tillage practices: A validation of the minNDTI strategy in the United States. *J. Soil Water Conserv.* 68, 120–131. <https://doi.org/10.2489/jswc.68.2.120>.